Dendrite engineering on xenon crystals

Marco Fell* and Jörg Bilgram†
Laboratorium für Festkörperphysik, ETH Zürich, 8093 Zürich, Switzerland
(Received 24 March 2007; published 20 June 2007)

The experimental work presented focuses on transient growth, morphological transitions, and control of xenon dendrites. Dendritic free growth is perturbed by two different mechanisms: Shaking and heating up to the melting temperature. Spontaneous and metastable multitip configurations are stabilized, coarsening is reduced, leading to a denser sidebranch growth, and a periodic tip splitting is found during perturbation by shaking. On the other hand, heating leads to controlled sidebranching and characteristic transitions of the tip shape. A deterministic behavior is found besides the random-noise-driven growth. The existence of a limit cycle is supported by the findings. Together the two perturbation mechanisms allow a "dendrite engineering"—i.e., a reproducible controlling of the crystal shape during its growth. The tip splitting for dendritic free growth is found not to be a splitting of the tip in two; rather, the respective growth velocities of the main tip and the fins change. The latter then surpass the main tip and develop into new tips. The occurrence of three- and four-tip configurations is explained with this mechanism. Finite-element calculations of the heat flow and the convective flow in the growth vessel show that the idea of a single axisymmetric toroidal convection roll across the whole growth vessel has to be dropped. The main effect of convection under Earth's gravity is the compression of the diffusive temperature field around the downward-growing tip. A model to explain the symmetry of dendritic crystals—e.g., snow crystals—is developed, based on the interaction of crystal shape and heat flow in the crystal.

DOI: 10.1103/PhysRevE.75.061603 PACS number(s): 81.10.Aj, 81.30.Fb, 64.70.Dv

I. INTRODUCTION

The growth of crystals into undercooled melt is a nonequilibrium process. It can lead to dendritic patterns as an archetype for pattern formation in natural processes far from equilibrium (see Fig. 1). Well-known examples of these patterns are snow crystals. Although they all look similar, two snow crystals have never an identical shape [1]. Every snowflake is a postcard with information about the atmospheric conditions in the environment of its growth.

The appearance of dendrites in cast metals has attracted strong interest in this topic: The microscopic dendritic structure arising when a solid grows from its undercooled melt influences the bulk properties of metals like strength, elasticity, ductility, etc.

Research in dendritic growth in the last decades has led to a considerable theoretical understanding of several aspects. In most theoretical models, the dendrite is assumed to grow unperturbed in an undercooled melt. Prominent experiments to prevent any perturbations were performed by Glicksman and co-workers [2,3] aboard the Space Shuttle. For the testing of steady-state theories, a microgravity environment is probably the best suited. Good agreement with the theories was found in experiments on different aspects like growth rate (e.g., Refs. [4,5]), tip shape (e.g., Refs. [6,7]), or sidebranching (e.g., Refs. [8–10]).

Two possibilities have been discussed about the onset of sidebranches: On the one hand, there is the widely accepted idea of *thermal noise* fluctuations (see Ref. [11]) that give rise to the initiation of sidebranches. On the other hand, there is another idea put forward by Holzmann [12] proposing a *limit cycle model* for growing dendrite as a dynamical system with an oscillating tip velocity. In the last years most theoretical work has been focused on the first idea and experiments were performed in this light.

Only a few experiments have been performed up to now under the aspect of transient growth conditions, and most of them have been done in a (quasi-)two-dimensional environment.

The influence of convective flow on the growth has been investigated experimentally and numerically. It has been shown in Ref. [13] that with convective flow the sidebranching occurs at a higher spatial frequency than without convection. The selection parameter σ^* [see Eq. (4)] was determined by Lee *et al.* [14] to be up to 50% higher.

An increasing number of numerical simulations in two and three dimensions have been performed in computational domains large enough to be comparable with experiments and theories. Phase-field models agree with observations of doublons (e.g., Refs. [15–17]) and theoretically predicted

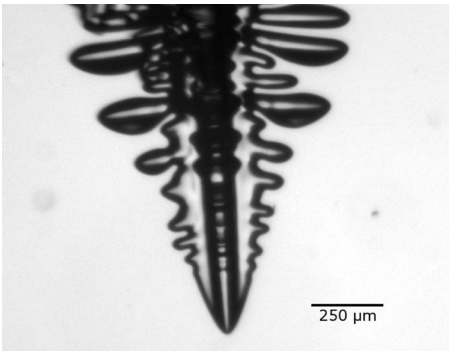

FIG. 1. A typical dendritic tip of a xenon crystal grown free from melt. The sidebranches grow on four sides (two of them point into and out of the picture plane), but they are not symmetric.

*Electronic address: mfell@phys.ethz.ch
†Electronic address: bilgram@solid.phys.ethz.ch

characteristic length scales (e.g., Refs. [18,19]).

The experimental work presented here focuses on transient growth, morphological transitions, and controlling. The main advantage of the setup used is the large volume of the growth vessel, providing the conditions for free growth in three dimensions, which means that the growth is not perturbed by the walls of the vessel. Based on this well-established fundamental, a series of new experiments have been performed with two different perturbation techniques applied to the growth of xenon crystals. They are described in Sec. III B.

This paper provides a hypothesis on a combination of the two ideas mentioned above: Thermal noise and limit cycle. The experimental findings described in Sec. IV furthermore provide the basis for this hypothesis and give rise to a technique of controlling the shapes of dendritic crystals during solidification, described in Sec. IV D. For a rough qualitative understanding of the diffusional and convective processes in the experiments, simulations (see Sec. V) have been performed.

During the work on this paper, the authors were told about a similar work by Dougherty and Nunnally [20] on transient growth on ammonium chloride dendrites.

It is worth mentioning that Gorbunov [21] reports on *dendritic melting* in superheated crystal volumes. In this case the metastable phase is solid and therefore convection can be excluded. The observed structures of the liquid regions in the crystal are hardly distinguishable from crystals in the melt described in this work. Various effects such as tip splitting and periodic sidebranches under periodically modulated superheating are found in dendritic melting.

II. PHYSICAL FRAMEWORK

A. Theoretical background

Melting is a first-order phase transition. Latent heat is released during freezing at the solid-liquid interface. The melting temperature (of a plane surface) is T_m, while the temperature in the melt, far away from the sold-liquid interface, is T_∞. The undercooling is $\Delta T = T_m - T_\infty > 0$. For comparison between different materials, the temperature field T is scaled with material constants, resulting in the dimensionless temperature field

$$u := \frac{(T - T_\infty)}{(\Delta T)}, \quad (\Delta T) = \frac{L}{c_p},$$

where (ΔT) is the unit undercooling, defined by L, the latent, and c_p, the specific, heat. The latent heat is transported away from the interface. This can happen either in a purely diffusive form or by convection involving mass transport. The former transport is described by the diffusion equation

$$\frac{\partial u}{\partial t} = D\,\Delta u, \tag{1}$$

where D denotes the thermal diffusivity. This relation holds for both the liquid and solid phases, with the respective diffusivity and specific heat parameters.

While one boundary condition is easily found—the temperature of the melt far from the solidification front is T_∞ or $u_\infty = 0$ in dimensionless units—the interface temperature requires a more detailed analysis [11]:

$$u|_{interface} = \Delta - \beta v_n - d\kappa, \tag{2}$$

where $\Delta = (T_m - T_\infty)\frac{c_p}{L}$ is the dimensionless undercooling far away from the interface. The second and third terms on the right-hand side describe the *kinetic factor* and the *Gibbs-Thomson* effect. Both prefactors β and d are potentially anisotropic. The fourfold anisotropy [in two dimensions (2D)] resulting from the crystallographic fcc structure of many metals is $d = d(\theta) = d_0[1 - \varepsilon_4 \cos(4\theta)]$, with $d_0 = \gamma T_m c_p / L^2$ the capillary length, proportional to the isotropic part of the surface energy γ, and θ the angle between the interface normal and a given crystallographic direction. In a three-dimensional description, the angular dependence term for d has a more complicated form (e.g., in Ref. [22]). The local curvature of the interface is κ. The more convex the solid surface is, the lower is the local interface temperature.

At the interface the energy conservation is given:

$$v_n = D(\nabla u|_{solid} - \nabla u|_{liquid}) \cdot \hat{\boldsymbol{n}}, \tag{3}$$

where v_n is the velocity normal to the solid-liquid interface that is proportional to the gradient in this direction. With this equation, dynamics enters the problem and it becomes a *moving boundary problem*.

Three implicit assumptions are made in the formulation of Eqs. (1)–(3).

(i) One component: The equations describe the problem in a pure single-component system. This work is restricted to this case.

(ii) Free growth: The initial temperature is T_∞ and it is kept at this value far from the growing crystal; no confinement effects influence the solid-liquid interface.

(iii) Symmetry: The thermal constants D and c_p are the same in both phases.

The last assumption has been made in many theoretical works (known as *symmetric models*) and is justified by the argument that the two parameters are at least in the same order of magnitude. Still, incorporating the different diffusivities gives a more complicated shape of the isotherms than a symmetric model which is usually assumed for convenience and therefore may lead to another system behavior (see Sec. II C).

Neglecting the kinetic and Gibbs-Thomson terms, Ivantsov [23] shows that a rotational paraboloid, growing into an undercooled melt, is a shape-preserving solution of the Stefan problem. He calculates the Péclet number $p = \rho v / 2D$, depending on the undercooling $\Delta = p e^p \int_p^\infty e^{-s}/s\, ds$, concluding that the paraboloid could grow with any radius of curvature ρ and growth rate v fulfilling this relation. Still the growth rate is observed to be unique for a given undercooling. The *selection problem* was attacked with the *maximum velocity hypothesis* by Nash and Glicksman [24], which was replaced by the *marginal stability theory* [25] that predicts a unique constant

$$\sigma^* = \frac{2Dd_0}{\rho^2 v}, \tag{4}$$

depending on material properties only. It was assumed that the growth takes place at an operating point at which the tip is just marginally stable. The numerical value for the so-called *stability constant* has been predicted in this theory, $\sigma^* \cong 1/4\pi^2$.

The *solvability theory* [26–28] incorporated the anisotropy of the surface tension. It was shown that this anisotropy has a major influence on the selection of a unique tip shape of the dendrite. Thermal noise was found to be amplified for selected frequencies [29]. From an initial wave packet, the amplified wavelengths grow with increasing distance from the tip. However, the strength of thermal noise was found to be about one order of magnitude too small for the measured sidebranch amplitudes.

In a fully three-dimensional theory for pattern selection for cubic anisotropic materials, Ben Amar and Brener [30,31] described the shape near the axisymmetric tip without noise using a perturbation ansatz

$$z(r,\phi) = -\frac{r^2}{2} + \sum A_m r^m \cos(m\phi),$$

in a cylindrical coordinate system with z along the main axis.

Furthermore, Brener found the shape of the dendrite tip to be of the form

$$z \propto |x|^{\beta},$$

with $\beta = 5/3$. This theoretical finding was confirmed by Bisang and Bilgram [32] to $\beta = 1.67 \pm 0.05$, with a prefactor $a = 0.58 \pm 0.04$. Brener's "arms" mean a fourfold-symmetric, integral structure of a dendrite, not the sidebranches.

Brener and Temkin [33] extended the theory away from steady state under consideration of noise-induced sidebranching. The amplitude of sidebranches of a nonaxisymmetric dendrite was found to grow exponentially:

$$A(z) \approx \bar{S} \exp\left(\frac{2(5/3)^{9/10}}{3\sqrt{\sigma^*}} z^{2/5}\right),$$

where $\bar{S} = 2k_B T^2 c_p D / L^2 v \rho^4$ denotes the dimensionless fluctuation strength. This amplitude has been verified by Wittwer and Bilgram [34].

B. Growth morphologies in steady-state growth

The morphologies of crystals grown freely from pure melt depend on undercooling Δ and surface energy anisotropy ε. A low anisotropy causes crystals to grow in a more isotropic habit *(seaweed morphology)* than dendrites with a preferred orientation. Brener *et al.* [35–37] developed *analytically* a phase diagram to classify the different two-dimensional growth morphologies. A morphology diagram for two- and three-dimensional free growth was found by means of *phase-field calculations* by Singer *et al.* [38]. Experimentally, transitions have been identified between the different morphologies. Dendrite tips have been observed to split, and the crystal has been found to continue to grow *temporarily* in seaweed morphology. It is assumed (e.g., in Ref. [39]) that these spontaneous transitions are induced by noise.

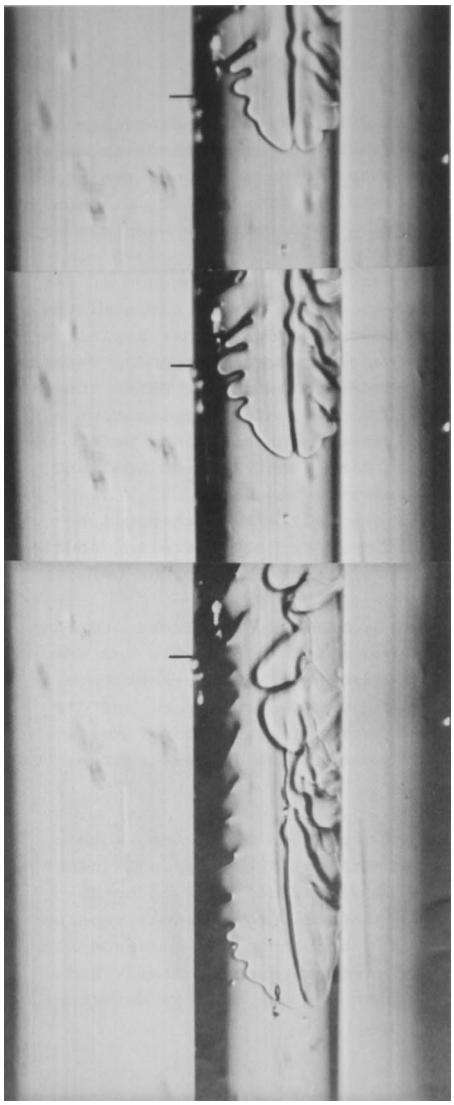

FIG. 2. The double fingers (doublons) are found in this SCN crystal growing along the glass capillary (courtesy of Lappe [42]).

Ihle and Müller-Krumbhaar [40,41] numerically found stable double fingers as another solution for the Stefan problem in two dimensions and assumed these *doublons* to be the building blocks of seaweed. In fact, these structures were observed almost 15 years before in an experimental work by Lappe [42] (see Fig. 2) and maybe in other works too, but they were not experimentally investigated until the experiments of Akamatsu *et al.* in quasi two dimensions [16]. Stalder and Bilgram [17] observed *dendritic doublons* in a three-dimensional growth vessel. The occurrence of Stalder and Bilgram's three-dimensional doublons was correlated with strong perturbations and did not lead to seaweed growth apart from a few rare cases. Dendritic doublons therefore have been identified as new growth morphology—besides the dendrites—existing for free growth. In recent works multitip configurations have been observed (e.g., in Ref. [34]).

Using a phase-field model Abel *et al.* [43] found that, depending on boundary conditions, solidification in a chan-

nel can lead to the growth of three or four fingers. The triplon as a steady-state configuration is not imposed by the symmetry of the walls; it consists of the cooperating symmetry-broken fingers growing with periodic boundary conditions (BCs).

C. Point attractor and limit cycle attractor

In early theories of the selection problem, the existence of a *limit cycle* for the tip growth parameters was suggested by Holzmann [12]. Two different diffusion constants for the solid and liquid phases are found to be necessary for this.

There are experiments that publicize an oscillating tip. Raz *et al.* [44] reported on this topic, as well as LaCombe *et al.* [3] and Liu *et al.* [45] in more recent works. They observed tip velocity oscillations and periodical sidebranching. Honjo *et al.* [4] observed both tip-stable and tip-oscillating types of dendrites, the latter showing highly correlated sidebranches.

In a recent work, Glicksman *et al.* [46] analyze the temperature boundary conditions and proposes the limit cycle as an alternative to the marginal stable interface under selective noise amplification.

On the other hand, an *operating point* of the system was proposed by Langer and Müller-Krumbhaar [25]. In the phase space of ρ and v, the system behavior is analyzed at this point of marginal stability. However, it is not clear how the system behaves in a small region around this point attractor for dendritic needle-crystal growth. It could show a noise-driven erratic behavior around the one special point, or it could be driven into a limit cycle [47], thus lock in to some oscillatory state.

Many experiments show a constant tip velocity. Glicksman *et al.* [2] and Bisang and Bilgram [5], for example, found the velocity to be constant within a $\leq 5\%$ margin over the observation time. Measurements of the stability constant σ^* result in unique values and are comparable to each other for different materials. The absolute values are in the region of the theoretically predicted $\sigma^* \cong 0.025$ [48].

In both the solvability theory and Brener's theory, thermal fluctuations are the reason for random sidebranching. This stochastic character for free dendritic growth had been confirmed in experimental observations: Dougherty *et al.* [8] reported that sidebranches show no periodicity and no apparent onset. Bisang and Bilgram's results [5] confirmed the random branching and found the distance where the sidebranches become visible to about 14 tip radii behind the tip, in agreement with Brener.

In this framework, the results of our experiments are an indication that both ideas—the operating point of marginal stability and the attractive limit cycle—should be considered and maybe extended with an unstable operating point for multitip configurations for a complete understanding of the dendritic growth.

III. EXPERIMENTAL SETUP AND PROCEDURES

The rare gas *xenon* is used as an experimental substance. It is an excellent model substance for metals since it solidifies in fcc structure and has a low melting entropy. Xenon grows with a rough surface, and the formation of dendrites is observed. The substance is liquid at 162 K (liquid nitrogen can be used as cooling substance) and transparent, allowing *in situ* observation of the growth. Unlike many organic substances, xenon forms a simple liquid and does not decompose at T_m. The purity is 99.9999%.

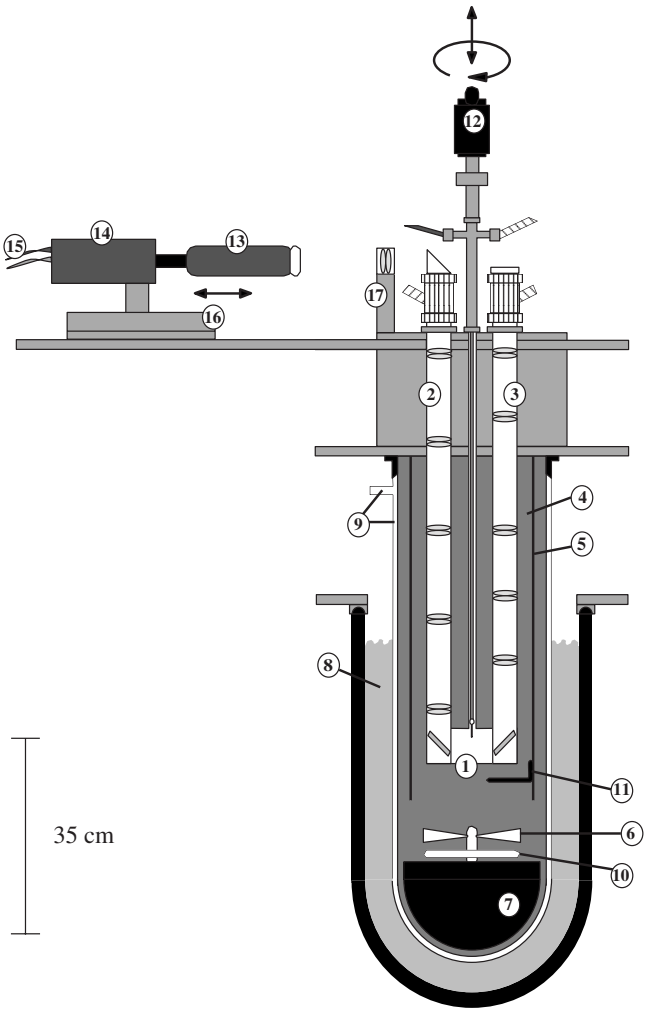

FIG. 3. Experimental setup: The growth vessel (1) is surrounded by isopentane (4). A stirrer (6), its oscillations damped by a large mass (7), and a tube (5) provide a laminar flow in the isopentane, which is cooled by nitrogen (8). The thermal insulation and heat transfer are provided by a helium-filled Dewar (9). A controller stabilizes the isopentane temperature in a closed loop with heater (10) and thermal resistors Pt-100 (11). By means of two periscopes illumination (3) and observation (2) of the growing crystal is done. They consist of a sequence of lenses with a flexible last field lens (17). The camera (14), on a moveable stage (16) and equipped with an additional zoom lens (13), is connected to a computer (15).

A. Cryostat and growth vessel

The experimental setup is based on our growth apparatus used in previous experiments [5], which provide a controlled growth environment. The complete setup is depicted in Fig. 3. It makes it possible to keep the temperature constant ($\Delta T \approx \pm 10^{-4}$ K) for hours.

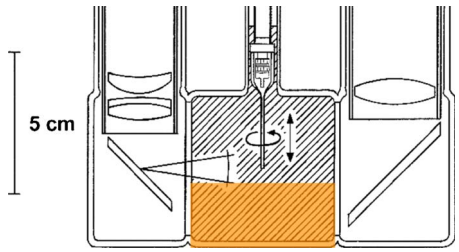

FIG. 4. (Color online) The growth vessel with the capillary (middle) and the observation and illumination periscopes to the left and right. The bottom is modified with a heating foil, typically powered 1 W.

The xenon is filled into a cylindrical growth vessel (Fig. 4) in the center of the heat bath. The volume of the vessel ($\approx$100 cm^3) is large enough to provide the conditions of free growth [6]. The solidification of a single crystal in the middle of the growth vessel is initiated by the *capillary injection technique* [49] from the top. Two thermal resistors Pt-100 measure the temperature in the vessel. The spatial orientation of the crystal growing out of the capillary is random and so is the projection of the crystal in the field of view. The turnable capillary permits to find a good projection angle and can be shifted vertically in a range of ±2 cm.

B. Heating and shaking

Two types of experiments have been performed on two almost identical setups as described above. Compared to the instantaneous parameter changes that are possible in calculations or by applying pressure to the melt, the temperature change is done in a more intuitive way by heating. There are specific modifications made for the heating and shaking experiments.

1. Heater

For rapid temperature changes, a heating foil is mounted on the lower half of the growth vessel (see Fig. 4). A heating power of about 1 W is used to increase the temperature of the xenon melt in the growth vessel. Too much heating results in massive turbulence in the liquid; therefore, we heat in intervals of ($t_{on} \approx 15$ s) and thereafter interrupt for ($t_{int} \approx 30$ s). Overall the mean heating power is about 0.2 W while heating up the melt and 0.1 W while keeping a temperature above the melting point. An initial undercooling in the range of 100 mK$\lesssim \Delta T \lesssim$400 mK is chosen, which corresponds to $2\times10^{-3} \lesssim \Delta \lesssim 8\times10^{-3}$ in dimensionless units. The application of heat pulses allows us to follow the heat flux as follows. The lower one of the two resistors in the growth vessel indicates a temperature rise about 30 s after triggering the heating pulse; the crystal tip (about 2 cm off the bottom of the vessel) reacts visibly another about 30 s later. This time frame has been confirmed in the fluid-dynamics simulations, described in Sec. V.

Heating procedure. A few minutes after the crystal has left the capillary, a steady-state temperature field is established and heating is started. The main restriction is that the temperature must not be kept above T_m for more than about 250 s. Otherwise, the crystal breaks off the capillary. Three temperature trends (shown schematically in Fig. 5) have been analyzed. The temperature rise from the initial temperature to the maximum in type (I) is measured to happen within about 10 s.

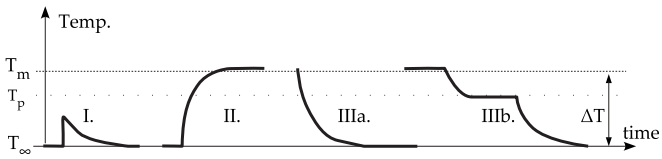

FIG. 5. Three different investigated temperature trends: (I) Short heating pulse below the melting temperature T_m, (II) heating to above T_m and melting, (IIIa) falling temperature without interaction, and (IIIb) falling temperature with a platform at T_p.

2. Shaker

The perturbation is generated by moving the crystal—located at the end of the capillary—back and forth. A piezo is built in the structure above the capillary (see Fig. 6). Its vertical movements are transformed into horizontal ones in a plane which turns with the capillary. The piezo elongation is amplified by the leverage from vertically 1.7 μm to horizontally $\sim$10 μm at the tip of the capillary.

Shaking procedure. The procedure for one run is as follows: After free growth for about 2 min the tracking (Sec. III C) is started where the crystal is slowly moved upwards at the same velocity as the tip grows downwards, $v_\perp$. Again 2 min later it is supposed that a steady-state diffusion field

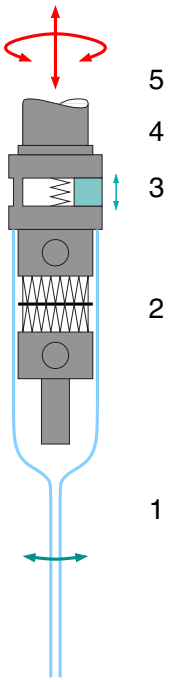

FIG. 6. (Color online) The capillary and the resulting degrees of freedom. (1) Glass capillary, (2) Peltier elements, (3) piezo and spring (the vertical movement is transformed to horizontal), (4) supporting structure, and (5) degrees of freedom of the crystal positioning.

and a convective flow have developed and then the perturbations are started. Typically the crystal is shaken for a time interval t_1 with a frequency f; then, it evolved freely for another interval t_2. The dimensionless undercooling of the 20 examined runs lies in a small range between 0.003 and 0.005.

C. Optical system and tracking

1. Imaging

The spatial resolution for the observation in both experimental apparatuses is diffraction limited by the optical setup to ≈ 1 μm. The growth process is recorded with a video camera at 756×581 pixels and additionally captured via a high-resolution charge-coupled device (CCD) camera at 1280×1024 pixels. The field of view is confined by the geometrical layout of the optical system. This is no restriction for heating investigations, since melting can prevent the crystal from growing out of this region. But for free growth and the shaking perturbations it is a serious problem: One needs to readjust the vertical position of the crystal in the growth vessel. By shifting the crystal in the melt the diffusion field is "washed away." A continuous tracking system minimizes this effect of position corrections. The camera position and the capillary z-axis position are used to keep the crystal tip fixed in the field of view.

This exact velocity $v_\perp$ is unknown at this time of the experiment because of the various thermal expansion coefficients of the capillary mounting between the liquid xenon at ≈ 160 K and room temperature where the driving is applied. It is determined *a posteriori* from the images by using an algorithm for the detection of the relative shift on the contours as described in the next section.

A pattern recognition software finds the position of the tip in a picture. The difference to a desired position is sent to a server that controls the linear positioners for both the capillary and the camera. This mechanism allows one to examine crystal growth over macroscopic distances for up to 40 min without noticeable, sudden perturbations.

2. Image processing

The contour of the crystal image as analytically accessible information is found by an edge-detection and contour-finding algorithm (see Ref. [50] for details). For the tracked crystals the challenge is the superposition of the images that has to be undone in order to find the temporal evolution of the shape and the tip positions. The idea of the algorithm is to take advantage of the morphological shape of the crystal that changes only a little between two images. The main tip grows and so do most of the sidebranch tips. The branchings, however, remain in their positions in the laboratory frame of reference. The later contour should thus enclose the former one like a glove. The question is, how to dress properly?

A measure for how well the glove fits is the sum of all distances between every point of a contour to the nearest point of the contour one time step before. This distance is minimized, and the resulting offset corresponds to the tip movement between the two images. Applying this algorithm for a sequence of some dozens to hundreds contours, it is possible to reconstruct the growth of the crystal part in the field of view. An example of how it works is shown in Fig. 7.

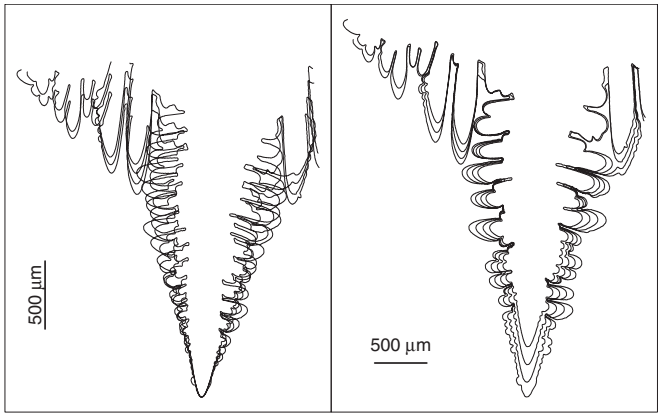

FIG. 7. The effect of the separation algorithm on a bunch of contours. Left: The contourlines are superimposed because of the stabilization of the tip in the field of view. Right: The *uncenter* algorithm shifts the contours and aligns them in the laboratory frame of reference. The growth rate of the crystal becomes visible.

Pixelated images have the inherent problem of spatial discretization. The "exact" solid-liquid interface is mapped onto pixels at a scale of about 1.3 μm per pixel (px) at best. This pixelation results in noisy signals and artifacts, and leads to large uncertainties, mainly for the two characteristic parameters of the radius ρ and the velocity v at the tip. A low-pass filter based on wavelet transformation (WT) is used to smooth the contours. Signal components with a wavelength $\lambda_c \approx 2$ px are cutoff (see Fig. 8).

D. Tip radius and local curvature

The determination of the radius of curvature ρ of a dendrite tip has been investigated in detail, e.g., in Refs. [51,52]. The technique of fitting a (polynomial) curve gives good results for the tip radius considering the contour up to a distance of about 5ρ behind the tip. The drastic change of the tip shape upon heating perturbations, however, does not provide a stable basis for fitting over 5ρ. Therefore we determine the tip radius by measuring the local curvature considering only about ten points in the tip region of the smoothed contour. A comparison of this method with the well-established ones agrees within 15% for unperturbed dendrites.

IV. RESULTS

A. Heating experiments

1. Controlled sidebranch initiation

a. Short pulse. Strong perturbations of the temperature field around the tip have been experimentally identified by Stalder and Bilgram [17] to trigger a morphology transition to a dendritic doublon. Fluctuations in the temperature field, caused by transient convective flows, were assumed by Wittwer and Bilgram [34] to be responsible for the "spontane-

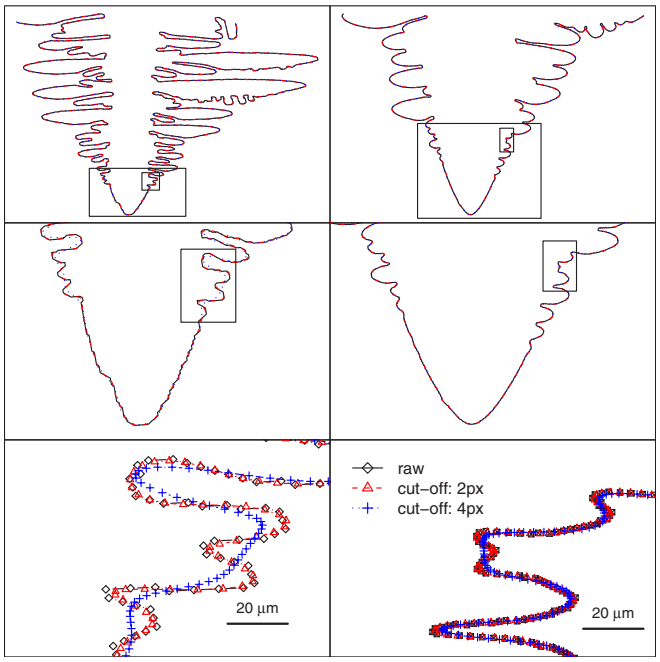

FIG. 8. (Color online) Two contours smoothed with wavelet transformations. Three zoom levels for each contour are shown; the panes are marked by rectangles. The original data points (◇) are compared to filtered data with a cutoff wavelength $\lambda_c \approx 2$ px (△) and $\lambda_c \approx 4$ px (+). While the first filter reproduces the original data from both sources video tape (left) and CCD camera (right) smoothly, the latter is lossy in both data sources.

ous" initiation of so-called *P*-type sidebranches (indicating *perturbation*-induced ones). By applying a sequence of single heating pulses (see Fig. 5, type I), it is possible to test this hypothesis. An example is given by the contours of a growing crystal in Fig. 9. In this case three heating pulses with a power of 0.9 W lasting for 15 s each, separated by a time interval of 360 s, were applied. The undercooling changed from 150 mK to 90 mK in less than 30 s and relaxed back to 150 mK in the next 300 s. This cycle was repeated twice more. In the image shown in Fig. 9, taken 1 min after the third heating pulse was measured, one clearly identifies two dominant sidebranches pairs: One at 2350 μm, the other at 1250 μm above the tip. A third pair of sidebranches has just emerged very close to the tip (150 μm), corresponding to about 5 tip radii, and is about to develop into a new dominant one, showing the characteristics of *P*-type sidebranches. Between the dominant sidebranches with equidistant spacing Λ, one observes random nonsymmetric sidebranches.

During the initiation of such a *P*-type sidebranch, the tip radius R grows to about 150%–170% and the tip velocity v drops to about 70% of their respective free growth value. Compared to the reaction of the tip velocity upon the heating pulse, the radius has a lag of about 25 s. Both values R and v relax back to the initial values within about 300 s. This *active* sidebranch initiation has been performed successfully with different undercoolings ΔT in the range from 100 to 300 mK.

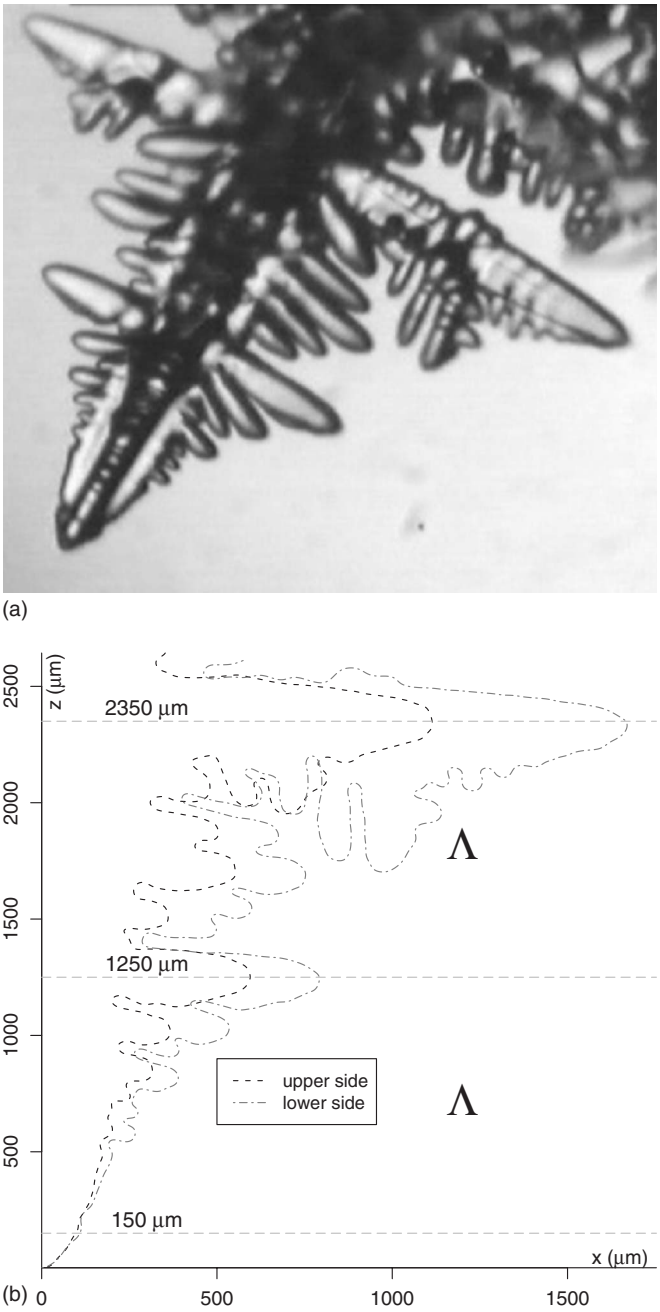

FIG. 9. Dominant sidebranches are initiated by a well-defined temperature rise. The contours on both the upper and lower sides of the crystal shown in the photograph are compared in the plot. The temporal intervals of 360 s between heating perturbations lead to spatial intervals $\Lambda = 1100$ μm of the dominant sidebranches. They are found on both sides at the same distance behind the tip; thus, they were initiated at the same time.

b. Melting-growth transition. In another sequence of investigations (see Fig. 5, type II) the xenon is heated to a temperature $T > T_m$. For the first seconds of temperature rise, this corresponds to the "short pulse" in the section above. But since the melting temperature T_m is reached within 5 min, the newly born *P*-type sidebranches cannot evolve and are melt away just seconds later. The melting regime is held for some minutes, causing more and more sidebranches

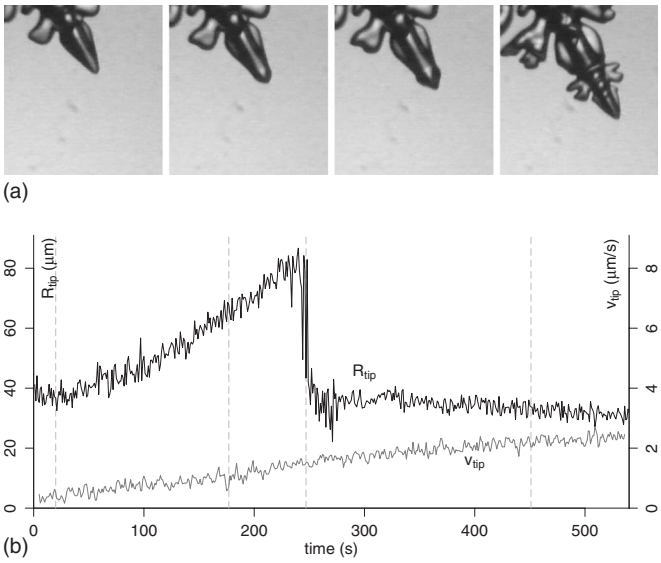

FIG. 10. Four snapshots of a dendrite tip growing during falling temperature. The smooth shape at the beginning becomes spherelike; the radius grows. Then suddenly a new sharp tip evolves and the sphere deforms to lobes at both sides that give rise to a characteristic sidebranch shape. The vertical lines in the plot of R and v indicate the corresponding time.

to disappear. The tip radius decreases to a steady-state value; the velocity becomes negative. When the temperature begins to drop (Fig. 5, type IIIa), the now smoothly shaped tip restarts growing. Four snapshots of this transition are shown in Fig. 10 with the corresponding values for the tip radius and the tip velocity as a function of time.

The tip shows an isotropical spherelike growth *with increasing radius* in the first minutes of falling temperature, while the growth rate v steadily increases. Within seconds, the tip deforms into a new sharp tip with a radius R corresponding to the current undercooling. The system falls into the basin of attraction for dendritic growth. During this sudden selection of a new operating point, symmetrical sidebranches are initiated. Focusing on the shape of these new sidebranches, it is easily seen that they are different from the P-type ones: They have doublon character, as can be seen in the last picture of the sequence in Fig. 10 and in the sequence in Fig. 11. The lower doublon constituent shows always an additional structure growing at a 45° angle to the main axis. This structure is further investigated in Sec. IV C. To clearly separate the sidebranches initiated during the change from melting to growth and because of their reproducible characteristic shape, they are called *T-type sidebranches*. This name indicates their origin in a transient temperature drop.

2. Evolution of the tip parameters

The main parameters to characterize steady-state dendritic growth (see Sec. II A) are the radius R and the velocity v of the main tip which show up in the inverse of the stability constant σ^*. The product R^2v has the dimension of a *solidification rate*. The temporal developments of these parameters are also useful to characterize transient states. They are plotted for typical temperature trends in Fig. 12.

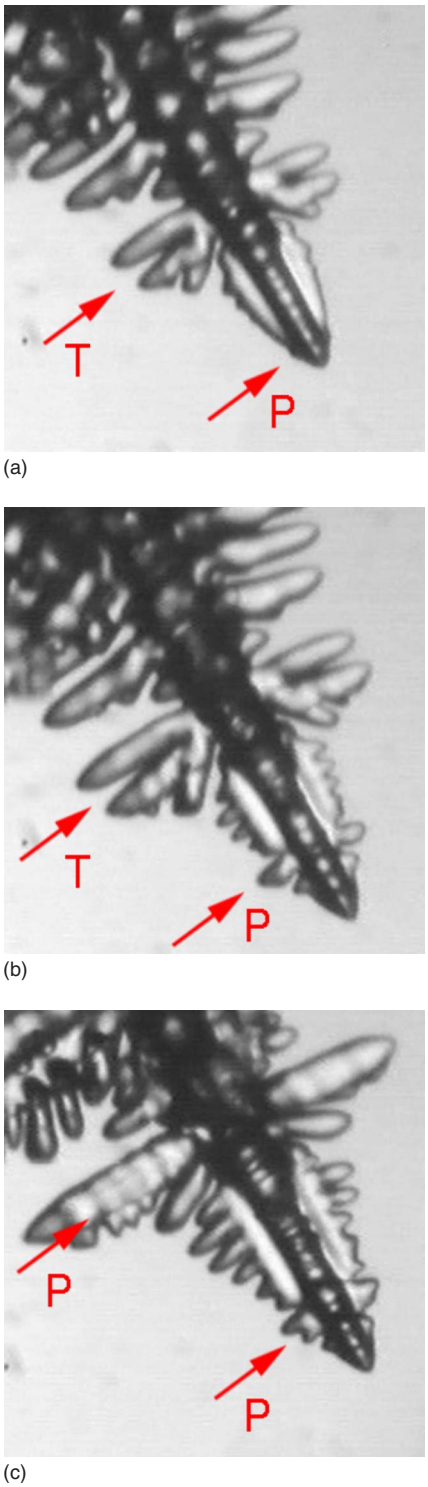

FIG. 11. (Color online) The characteristic shapes of the new *transition-initiated sidebranches* (T-type) in comparison with the P-type sidebranches. (a) The dominant doublonlike T-type sidebranch was initiated by the falling temperature transition. A heating pulse caused a P-type sidebranch starting at the tip. (b) Two minutes later, the T-type sidebranch structure has grown larger; the doublon character is still visible. The P-type sidebranch has become dominant in its surrounding. (c) The same crystal 5 min later shows the now dominant P-type sidebranch and the beginning of another P-type branch. The T-type sidebranch has left the field of view.

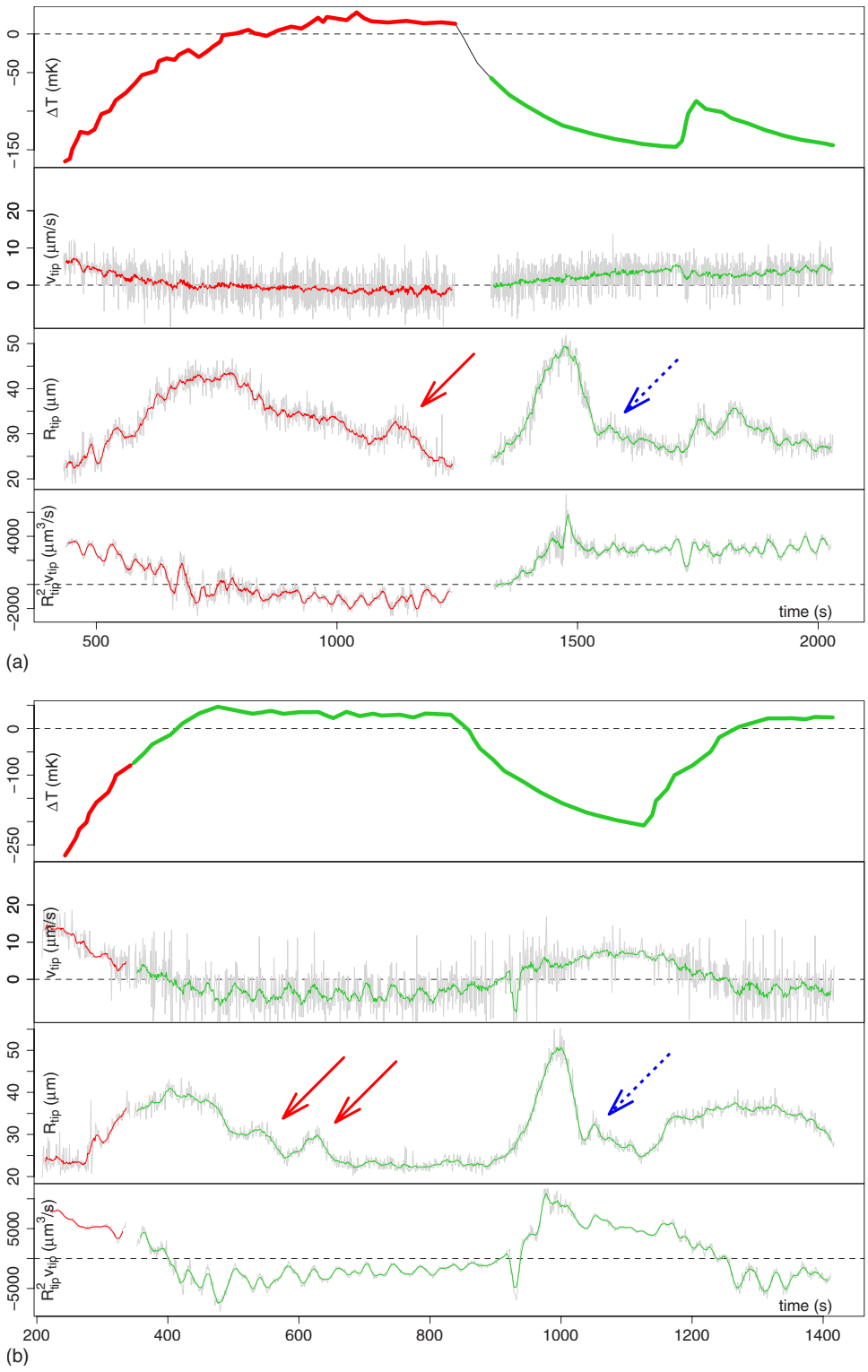

FIG. 12. (Color online) The temporal evolution of the characteristic parameters of the main tip. The temperature trends I, II, and IIIa (Fig. 5) are shown. The plain arrows indicate disappearing sidebranches during melting, the dotted ones typical doublon birth in *T*-type sidebranching.

a. Tip velocity. The tip decelerates for rising temperatures. As long as the temperature remains above the melting temperature T_m, the tip shrinks, and hence its velocity is negative. The tip velocity accelerates with falling temperature as expected. It has been found to react almost instantaneously on changed temperature in accordance with the Koss *et al.* [53] experimental and Steinbach *et al.* [54] numerical observations. The transitions from growing to shrinking are smooth.

b. Tip radius. The radius of the tip, on the other hand,

increases after any perturbation. A rising temperature, caused either by a single pulse or by the initiation of a melting phase, always triggers the formation of sidebranches (*P*-type). An indicator for this formation is the temporary increase of the tip radius. Once the temperature T exceeds T_m, the radius becomes smaller until it reaches a steady-state value about 5 min later. This constant value was observed in a different experimental setup by Glicksman, Lupulescu, and Koss in microgravity [55,56], before the melting crystal became so small that capillarity effects set in. The bulges one observes during the melting phase [plain arrows in Figs. 12(a) and 12(b)] are caused by a shrinking sidebranch disappearing at the tip. This sidebranch is not necessarily a former *P*-type sidebranch.

The sharp rise in the tip radius and the even sharper drop to a new value, followed by another small bulge [dotted arrows in Figs. 12(a) and 12(b)] is characteristic for the *T*-type sidebranching in falling temperature. It is remarkable that the first sharp drop in the tip radius takes place when the undercooling $\Delta T(t)$ is at $(0.69\pm0.055)\Delta T$. The small bulge, indicating the second finger of the doublonlike sidebranch structure arising, is at $(0.79\pm0.064)\Delta T$. These values are measured for undercoolings of about 160 mK. In another run with about 250 mK undercooling, this hysteresis effect was found at $(0.60\pm0.048)\Delta T$ and $(0.72\pm0.057)\Delta T$, respectively. No difference in the maximum tip radius could be found for different undercoolings. In all cases the radius reached between 48 and 55 μm.

The observation of a dominant sidebranch as the reaction of a change in the growth environment is consistent with a similar observation of Koss *et al.* [53]. Because of experimental limitations, they could not see a maximum-area projection of their crystal and could not find the symmetry of the induced *P*-type sidebranches.

c. Solidification rate. While the value R^2v near the tip changes from a *growth* rate to a *shrink* rate during the heating phase, it mirrors the behavior of the tip radius R in the transition back to growing. In a recent paper, Steinbach *et al.* [54] reported on the evolution of these values during transient growth simulations. They found the tip velocity to respond almost instantaneously on changed temperature and to "overshoot" initially. After this abrupt change, the velocity slowly approached the steady-state value. The variation of the solidification rate showed a constant value except for a pronounced spike immediately following the temperature change.

In the results presented in Fig. 12 the temperature does not change instantaneously as in the numerical experiment of Steinbach *et al.* The spike in the solidification rate is correlated with the increase in R during the falling temperature. It can be seen in Fig. 12(a) that the solidification rate is essentially constant after the spike at $t=1500$ s. Even during the short heating pulse phase at $t>1700$ s, the solidification rate remains at about 3000 $\mu m^2/s$. In Fig. 12(b) the shrink rate during melting is found to show a good stability at about -2500 $\mu m^2/s$.

The observations of a growing tip radius during the first moments in the transition to growth and the emergence of thin tips is also found by Dougherty and Nunnally [20].

B. Shaking experiments

1. Inclination and twist of the growth axis

In a total of seven different runs a misorientation in the crystal has been observed after start (in five cases) or stop (one single case) of the periodic perturbations. One event has been found after an unidentified accidental perturbation of the tip. Inclinations in the growth axes are measured in the observation plane between $1.5°\pm0.2°$ and $8.2°\pm0.2°$. The inclinations appeared when the oscillation plane was the same ($\pm10\%$) as the observation plane and also when the planes were perpendicular ($\pm10\%$) to each other. No dependence on the angle between the observation plane and the plane of movement has been found. While in some cases the main axis was restored after the perturbation was switched off, the inclined growth axis persisted in others. A closer look at both of these types (see Fig. 13) reveals two different mechanisms: (i) The more distinct inclinations are caused by a sequence of cascading tip splittings (see Sec. IV C) that preserve the main axis. The errant tips can switch back—i.e.,

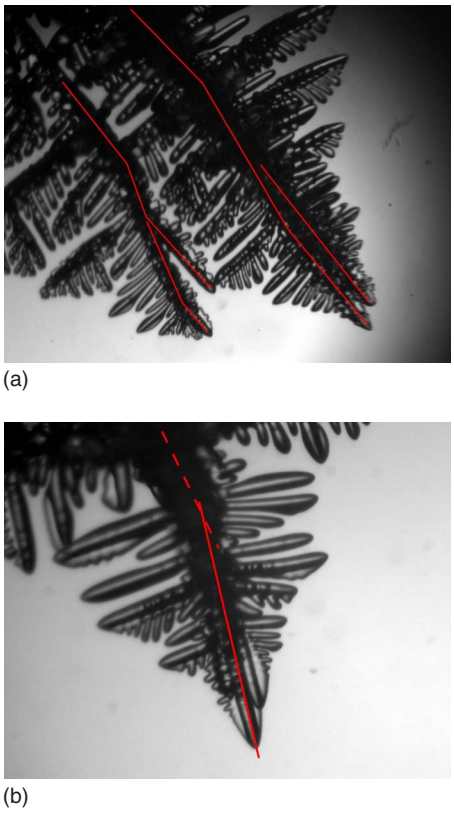

(a)

(b)

FIG. 13. (Color online) Different types of inclinations. (a) The tip performs a series of tip splittings, but preserves the original growth direction. This allows the growth direction to switch back to the original one, either spontaneously or after stopping the perturbation. (b) The crystal suffers a change in the direction of its ⟨100⟩ main axis. The original orientation is shown by a dashed line, while the plain line shows the new growth direction, the angle is about 11° before the geometrical correction.

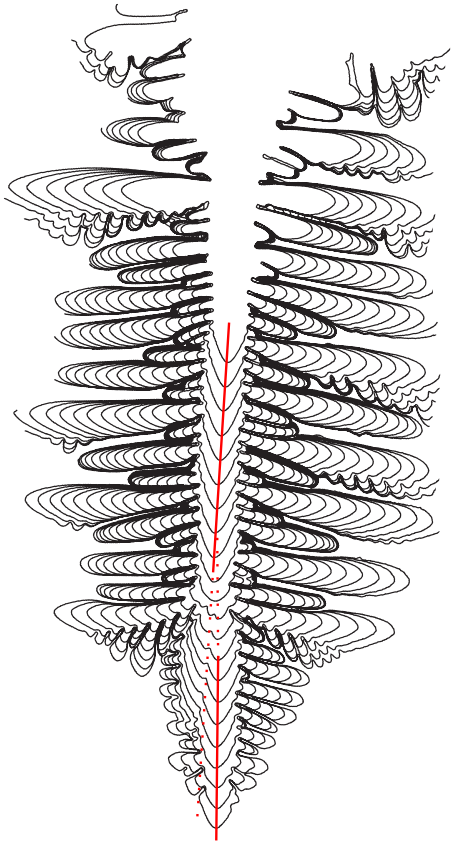

FIG. 14. (Color online) A sequence of contours showing the temporal evolution of an inclination. The change of the direction of the growth direction happens as the tip splits. After this tip instability, another main tip dominates the growth, but its ⟨100⟩ axis is inclined by about 2° to the axis before.

stop splitting and continue growing along the main axis. (ii) The other less pronounced inclinations do in fact change the main growth axis. It is important to keep in mind that these inclinations are not "breaks"; i.e., the crystal does not break at some point in its structure. Rather, at some time, the tip changes its growth direction. A sequence of contours showing the temporal evolution of the inclination is plotted in Fig. 14.

A second change in the growing crystal structure is observed as a *twist* along the main axis. Unfortunately only one single instance of this twist has been found up to now. It is shown in Fig. 15(a). In the upper part of the picture, the crystal is oriented in such a way that one clearly identifies a bright line in the crystal structure center. The light traversing through the melt is refracted at the solid-liquid interface because of the difference in the refractive index. The larger the angle between the interface normal and the light beam, the more is it refracted and the darker appears the structure.

Above the marker line one cannot see any of the fourfold symmetric fins on the trunk; they appear dark. Below the marker, there are fins visible and the bright trunk is slightly shifted. The twist occurred during growth, when the tip was at the position of the marker. A possible explanation for this visible "failure" is a rotation of the crystal around the ⟨100⟩ growth axis as depicted in the schematic cross section in Fig.

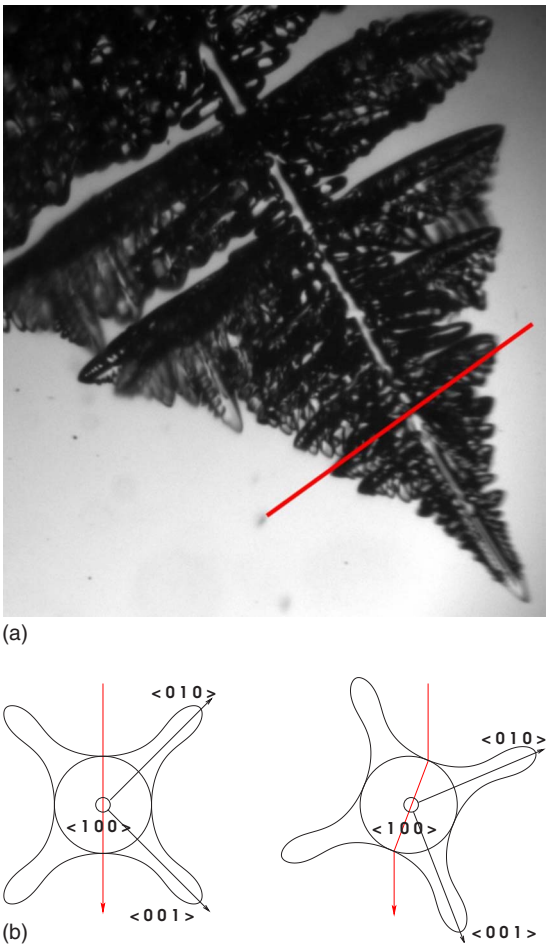

FIG. 15. (Color online) (a) The crystal is oriented in such a way that the light line of the trunk is clearly visible above the marker (the light is passing through the most inner part of the dendrite). Note that below the marker the trunk line is shifted while the fins are identifiable. The two gaps in the sidebranch structure separate one dominant *P*-type branch from its random neighbors. It was triggered by the start of the perturbations almost 6 min before the picture was taken. (b) The scheme shows the path of light through the trunk and the orientation of the crystallographic main axes before and after the twist.

15(b). The twist was found after the orientation of the projection was changed; i.e., the capillary was turned. In earlier experiments, a fast turn of the crystal in its melt caused tip splittings (similar to Stalder's doublons) but no twist. We think therefore that the shear flow of liquid along the surface of the tip during the small turn can be ruled out as the only reason for the twist. More probably, the combination of an unstable microscopical interface, caused by the perturbation by shaking and the shear flow due to the capillary turn at the same time, might lead to the formation of twins and thus to a twist or inclination in the crystal structure.

2. Morphology stability

Without any changing of the growth environment, spontaneous formations of multitip configurations evolving from a dendritic tip have been observed before [57,58]. These

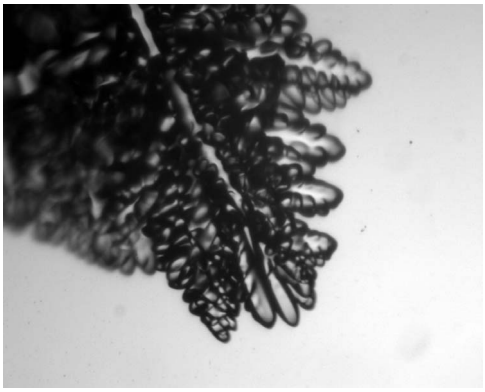

FIG. 16. A multitip configuration showing that three main tips are growing close to each other. This multiplon was stable for the following more than 20 min.

multiplons (see Fig. 16) decayed within 30 s to 3 min to a dendrite again.

In the 20 examined sequences with shaking perturbation, 18 tip-splitting events at the main tip have been found. Three of them showed up spontaneously while no perturbation was applied; they decayed within 60–200 s. Another three showed up during oscillation and also decayed about 200 s after the perturbations were stopped. Most tip splittings were induced by starting the perturbations as one could expect. There were six tip splittings found that led to a doublon or to a multiplon (by a sequence of splittings) that was stable as long as the shaking perturbations were continued for up to 1500 s. The applied perturbations covered a large range from 1/60 Hz to 2 Hz and no influence of the frequency was found.

C. Cascading tip splitting

In experiments with both kinds of perturbations—melting and shaking—tips growing in an oscillating mode have identified. This means that either a *periodic splitting* or a *periodic sidebranching* in the tip region took place for up to 5 min. While the sidebranching leads to structures on all sides of a growing tip, the splitting leads to new tips with new growth directions. These tip splittings have to be distinguished from multiplon formation where the multiple tips preserve (almost) their main growth direction. The cascading splitting reported here takes place periodically, once to the one side, then to the other (say, alternatively to the left and right). Figures 17(a)–17(c) show examples for the mentioned events. The first (a) and last ones (c) were found in the shaking, the middle (b) in the melting experiments.

While the cascading tip splitting as in (a) never showed up spontaneously but always in correlation with shaking, (b) was found to be characteristic for the *T*-type branching after a transition to low temperatures and (c) could be found as reaction upon perturbation as well as spontaneously.

The periodic early sidebranching can also be interpreted as a tip splitting into three (or five considering the 3D shape), whereas two (four) bulges on the two (four) sides of the tip degenerate into sidebranches.

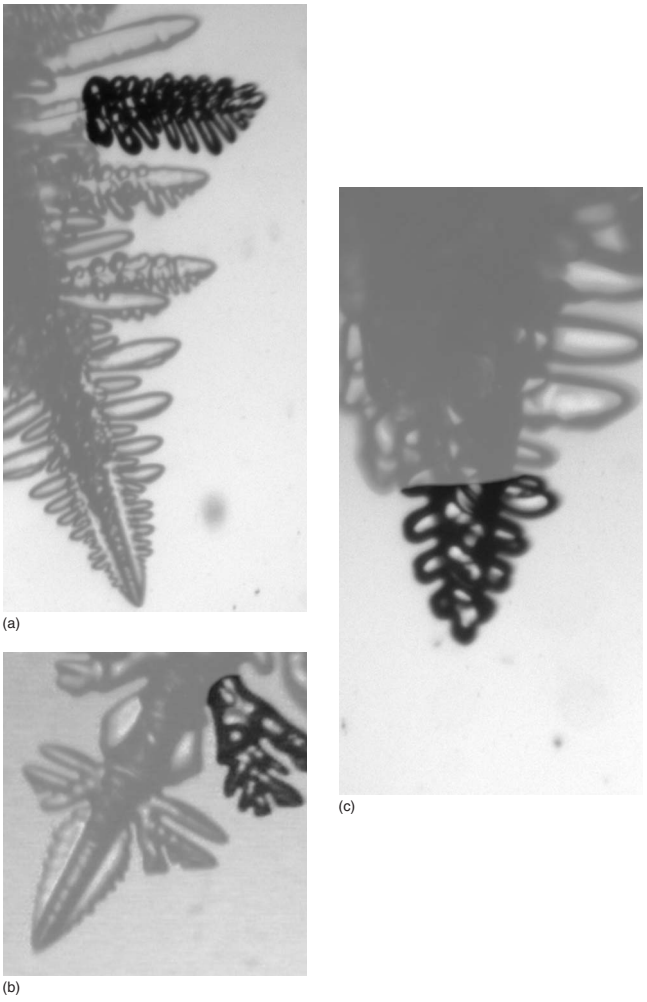

FIG. 17. Alternating tip splitting, *cascading*, on three different situations. (a) The sidebranch tip shows a sequence of periodic tip splittings in alternating directions. The final direction is parallel to the initial one. (b) The 45° structure is typical for *T*-type sidebranches. Its tip performs a periodic alternating splitting. (c) One tip in a multitip configuration. It shows periodic sidebranching alternating to the left and right.

The temporal evolution in the highlighted regions seen in Fig. 17 is depicted in the contours in Fig. 18. The visually observed sidebranch tips in a cascading region have been marked when they were clearly formed; then, the positions were tracked backwards in time. The contours have been rotated and stretched in order to make the shapes appear in true relations.

The angle between the two new tips is found to be constant during such a splitting sequence, typically 45° as shown in Fig. 19. The consecutive splittings into ⟨100⟩ and ⟨010⟩ directions results in a trunk along the ⟨110⟩ axis. Similar structures have been found by Henry, Minghetti, and Rappaz [59] in aluminum alloys.

The cascading tip-splitting mechanism seems to be a universal concept. Utter *et al.* [60] report on it at the main tip in directional solidification, and Karma and Lobkovsky [61] found it in a phase-field simulation on crack propagation.

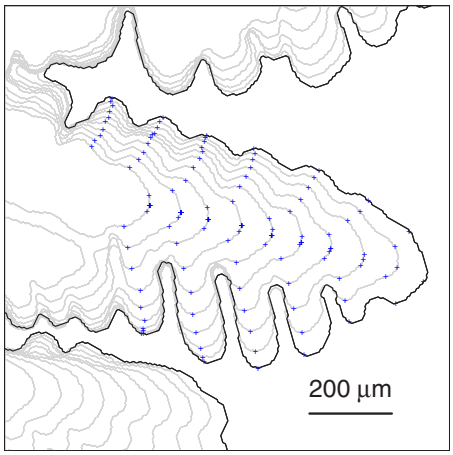

(a)

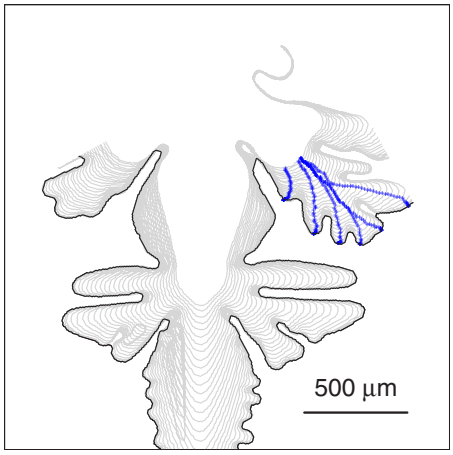

(b)

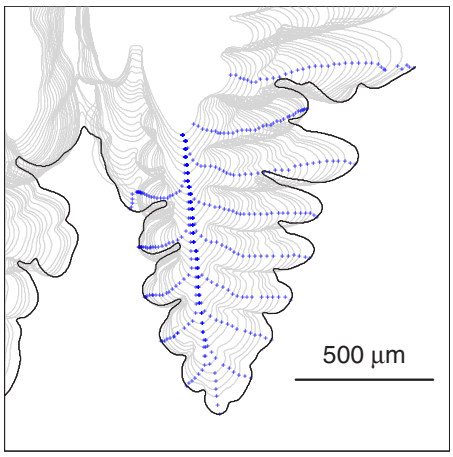

(c)

FIG. 18. (Color online) The same tip splittings shown in Fig. 17 are plotted in the temporal evolution. The tips of the branches are marked on the last contour and tracked back in time. The time interval between the points is 10 s.

D. An application: Dendrite engineering

1. Symmetry

The controlled initiation of sidebranches of both types *P* and *T* (described in Sec. IV A 1) is observed to give rise to a pair of sidebranches synchronously. In fact all these "pairs" are double pairs, one in the image plane and one perpendicular to it. Comparing the two perpendicular pairs by turning the capillary by 90°, fourfold-symmetric sidebranching is observed as shown in Figs. 20(a) and 20(b). The superposition of the four outlines is shown in Fig. 20(c). The first lobes on all four contours show an excellent correlation, while the more evolved sidebranches (they have grown for a longer time since they symmetrically have emerged) start to be influenced by random processes, independent from each other. Plotting the local curvatures of the contour starting at the tip [Fig. 20(c), bottom] gives a more quantitative way to demonstrate the symmetric shape of the sidebranches on the four fins. The maxima and minima coincide over a large distance.

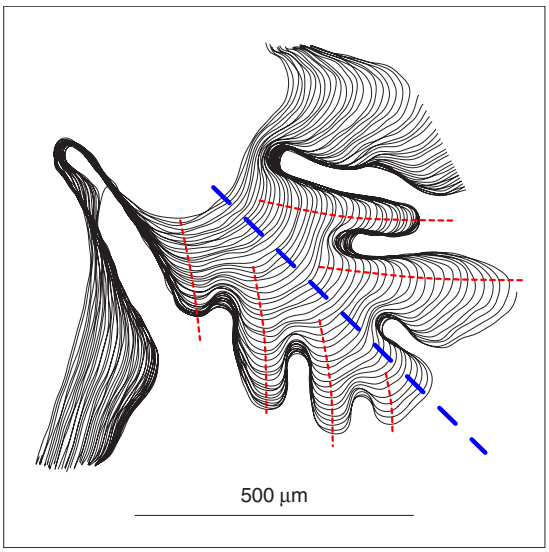

FIG. 19. (Color online) A detail of the typical *T*-type sidebranch structure. While the main direction (dashed boldline) of this structure is 45° against the dendrite tip's ⟨100⟩ axis, each alternating branching leads to second order branches again in a 45° angle (dashed thin line).

By periodically applied cycles of heating until melting smoothed the crystal and transitions to growth, shapes as shown in Fig. 21 are obtained. The symmetry is visible in a 45° projection [Fig. 21(a)]. The right-hand side of the crystal in this picture shows longer sidebranches. Figure 21(b) shows another crystal in maximum-area projection. There are *higher-order branchings* (i.e., branching off the sidebranches) clearly identifiable, occurring on both sides of the crystal synchronously, despite the more than 500 μm distance in between ($\approx$20 tip radii).

2. Transient tip shapes in melting

The transition from melting to growth leads to the spherelike tip and the *T*-type sidebranches described in Sec. IV A 1 b. If the temperature drop is slowed down [heating is used to stabilize it at $T_m > T_p > T_\infty$ for some minutes; see Fig. 5(IIIb)], a rather spearlike triangular tip with straight sides grows. A comparison with the heating-pulse *P*-type branching and with the spherelike shape is shown in Fig. 22. While the pulse lets dominant *P*-type sidebranches grow, the

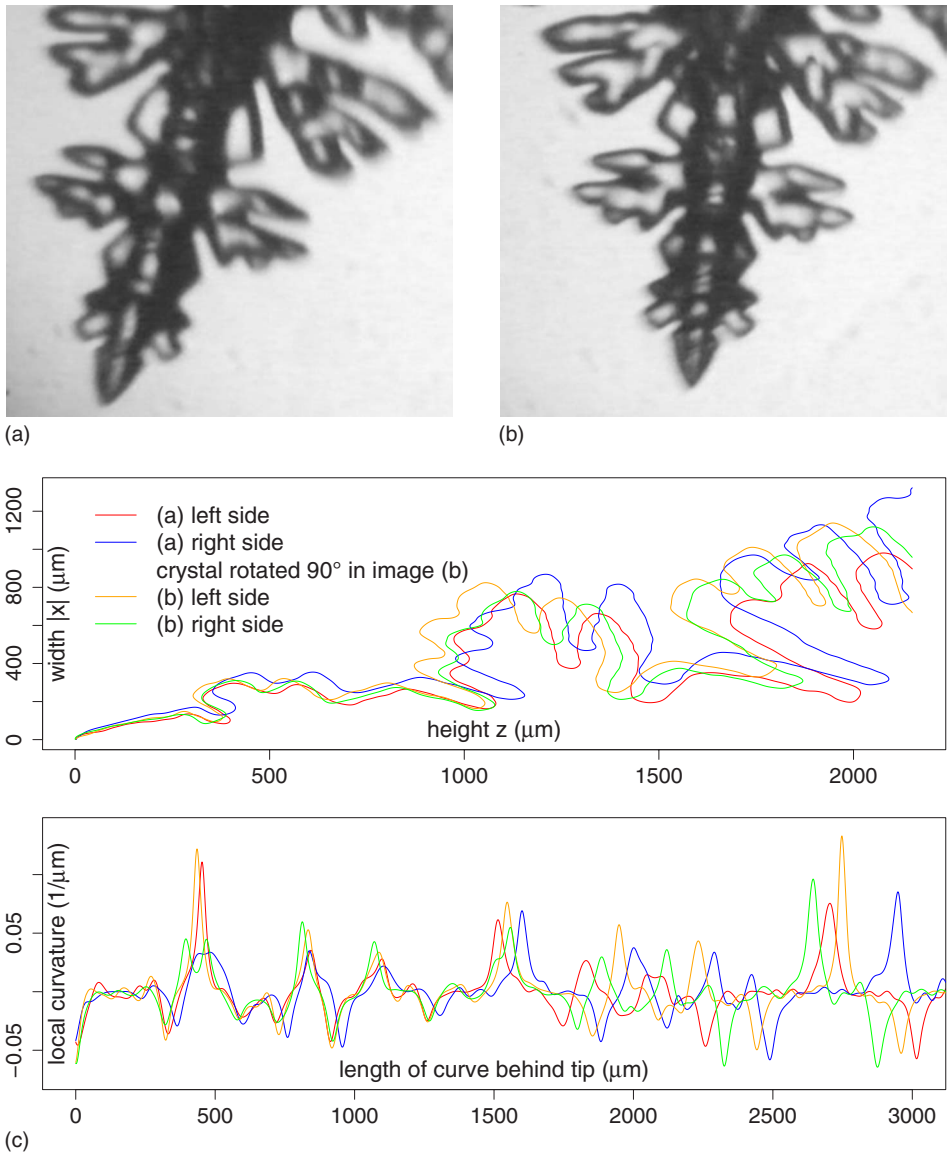

FIG. 20. (Color online) A symmetric tip viewed from two perpendicular angles. The images (a) and (b) show a symmetric shape. The four outlines are plotted in the upper panel of (c). The shapes are almost the same on all four sides. For both perspectives (a),(b) the right-hand side—i.e., the lower part of the dendrite—grows a little faster. The local curvature of the same contours, plotted against the contour length behind the tip, is shown in the lower panel of (c). The curvatures are highly correlated for the first 1.5 mm; then, the asymmetric growth makes the before coincidental maxima and minima lose coherence.

spherelike transition gives rise to the typical *T*-type sidebranching with doublon character. The straight sides of the spearlike tip become unstable against the Mullins-Sekerka instability.

The difference between spherical and triangular transition of the dendrite tip is also seen in the plot for the characteristic parameters (Fig. 23). Compared to the *T*-type branchings in Fig. 12 the sharp drop does not show up and nor does the distinctive bulge indicate the second partner of the doublon. The tip gradually becomes thinner over a lapse of about 150 s while the velocity increases. These two characteristics together lead to the triangular shape.

3. Sidebranch initiation and coarsening

One of the characteristic features of dendritic growth patterns is the sidebranch spacing. The controlled sidebranch initiation by temperature changes, described in Sec. IV A 1, allows one to modify this feature. A comparison between a freely grown dendrite (a) and a shaken one (b) in Fig. 24 reveals another modification of the sidebranch geometry. Both dendrites were grown at the same undercooling of $\Delta \approx 0.005$; nevertheless, they show a difference in their sidebranch arrangement. The sidebranch growth for the free dendrite obeys Brener's law for the amplitude of sidebranches [33], as confirmed by Wittwer and Bilgram [34]. The tip region is smooth, having the shape of a $|x|^{5/3}$ curve. Sidebranches start being visible at a distance $\bar{z}_{SB}$ of about 10–15 tip radii behind the tip, in accordance with Ref. [5]. Shortly after the formation of sidebranches, coarsening sets in and only a few dominant ones continue to grow, while their neighbors vanish.

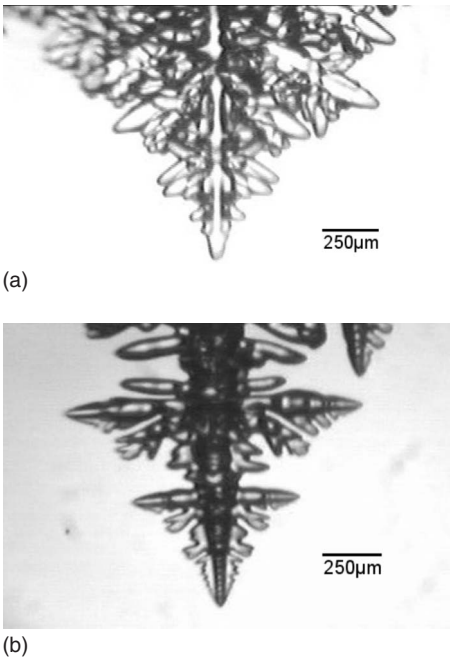

FIG. 21. Two symmetric crystals viewed (a) from a 45° angle and (b) in a maximum-area projection. The symmetric sidebranches show higher-order branchings occurring simultaneously even though they are about 20 tip radii separated.

For a shaken dendrite the sidebranches start growing at the very tip. This is an indication for perturbation-induced *P*-type sidebranches. There is no clear distinction between dominant and vanishing sidebranches in the region up to about 1000 μm. The area filling factor—i.e., the solid/liquid ratio within the dendrite envelope—seems to be higher than for the free dendrite.

The superposition of the two geometrically corrected contours in Fig. 24(c) shows that the envelope of the shaken dendrite has more a triangular shape with straight sides, whereas the envelope of the free dendrite is curved. A rough estimate of the angle of aperture of the envelopes at the tip gives about $35° \pm 5°$ for the free dendrite and about $70° \pm 5°$ for the shaken one in the lower region of about 1000 μm. The sidebranch amplitudes of the shaken crystal are in fact larger than the ones of free dendrites. The dominant sidebranches of the free dendrite—that could "free itself from its surrounding"—surpass the shaken ones and have larger amplitudes from about 1200 μm behind the tip.

The temporal evolution of sidebranches is shown in (d) and (e). On the shaken dendrite (e), the sidebranch spacing λ is wider, they start earlier, and the coarsening process is less effective than on the free dendrite (d). Up to a height of 1000 μm, the variance of the sidebranch amplitude is smaller than for free growth.

4. Area

Figure 24(c) brings us back to the idea of a volume-filling factor discussed in Ref. [7]. The projection area of the shaken dendrite resembles a triangle. A simple model for the area A of such a triangle leads to

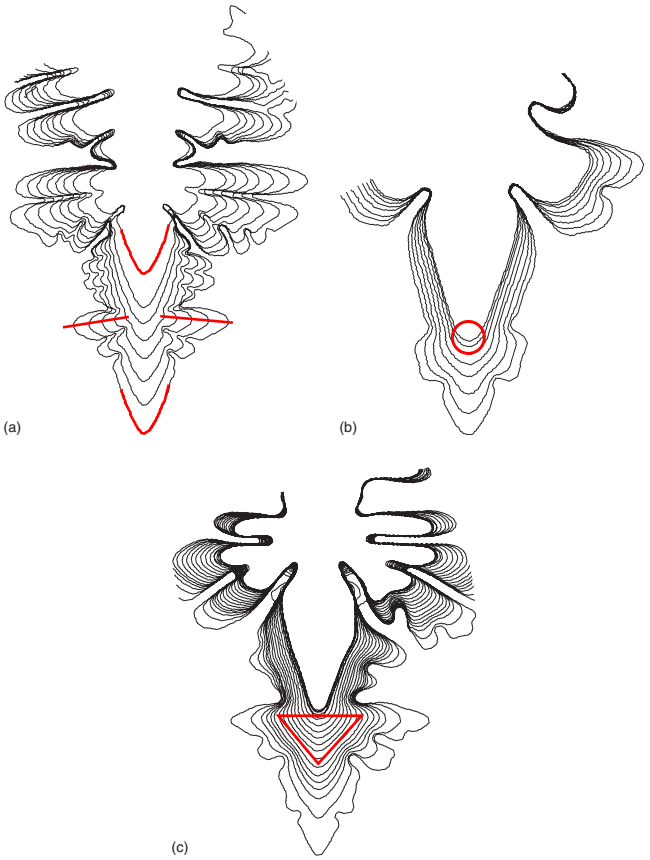

FIG. 22. (Color online) Three possibilities for tip shaping: Heat pulse, free falling temperature, and slowed temperature drop lead to different tip shapes and therefore different sidebranches. (a) The heat pulse produces a *P*-type sidebranch; the tip shape remains unchanged. (b) A falling temperature transition results in a temporary spherical growth and to *T*-type sidebranches. (c) When the temperature drop is slowed down, the tip evolves to a triangular shape and the sidebranches evolve later, compared to (b). The contours show the crystals outlines in 50-s intervals for (a) and (b) and 100-s intervals for (c).

$$h = v_{tip} t, \tag{5}$$

$$w \approx 2 v_{SB} t \sim 2 \frac{v_{tip}}{2} t = h,$$

$$A \sim \frac{hw}{2} \sim 0.5 h^2, \tag{6}$$

where h is the height along the z axis, w the width along the x axis, v_{tip} the main tip velocity, and v_{SB} the sidebranch tip velocity. The ratio of the two velocities was found in Ref. [62] to be $v_{SB}/v_{tip} \sim 0.5$.

The measured area as a function of h^2 is seen in Fig. 25 for 12 different dendrites. The prefactor is a measure for the area filling factor $A = \beta h^2$. The prefactor β for 11 sequences from 9 different freely grown crystals is $\beta = 0.210 \pm 0.035$, while the same prefactor for 8 sequences from 3 different shaken crystals is significantly larger, $\beta = 0.365 \pm 0.020$. Different frequencies of perturbation have been applied, 1/40,

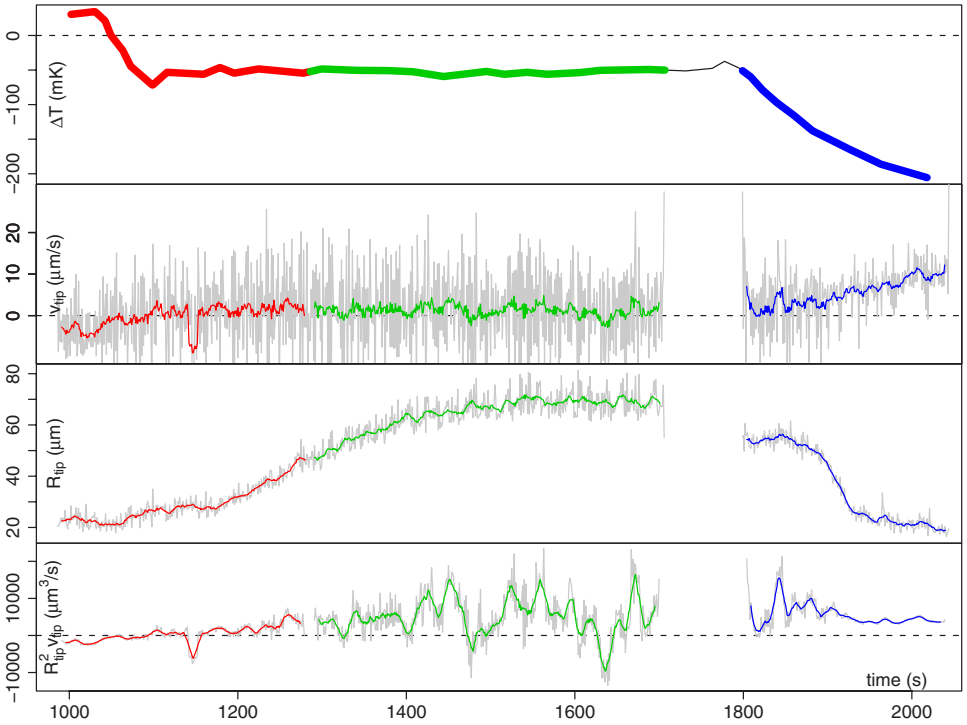

FIG. 23. (Color online) The temporal evolution of the characteristic parameters of the main tip. The temperature is stabilized at $\Delta T \approx 50$ mK for almost 700 s. The velocity is about 2 μm/s during this period, and the radius grows to a stable value. Once the temperature is allowed to fall towards T_∞, the velocity increases and the radius decreases without the sharp drop seen in Fig. 12.

1/10, and 2 Hz, and the range of undercooling is 100 mK $\lesssim \Delta T \lesssim 250$ mK. No influence has been found. In the simple model of a filled triangle, about 40% of the area is solidified in free growth, whereas the shaken dendrites fill the triangle to more than 70%.

V. SIMULATIONS

A. Setup

For a qualitative analysis of the thermal fields in the growth vessel, simulations over the complete domain have been performed. The size of about $5 \times 5 \times 5$ cm^3 prevented us from using microscopic modeling for computational reasons. We supposed that for qualitatively reasonable results it is sufficient to solve the classical fluid dynamics equations using a finite-element method. The surface of the simulated crystal was kept at the melting temperature T_m; the outside of the vessel and the heating foil was kept at T_∞. The material parameters used are shown in Table I.

Two meshes with a different lower limit for the element size (both much smaller than the capillary diameter of about 220 μm; see Table II) have been compared for steady-state situations and showed no significant differences in the results. The mesh with about 176 000 elements is used for the simulation of the transient fields. The boundaries of the used mesh is shown in Fig. 26. The crystal has a tilt angle ($\approx 20°$) against the vertical that is typically observed in the experiments. The symmetry is broken, and thus the whole domain has to be solved.

B. Convective flow

In Earth-bound solidification experiments in melt, there is natural convection. It has been an open question as to how strong this convective flow is in our growth vessel.

1. Experimental observations

Experimentally it was possible in two cases to observe single dust particles in the liquid xenon in the focus plane. They were about 5–10 μm in diameter, and the maximum speed in one sequence was measured to be of an order of magnitude of 0.5–0.7 mm/s. This value is supposed to be of the order of magnitude of the convective velocity in the experiment.

2. Simulations in 3D

The simulation without convection—i.e., calculating the diffusion equation only [Fig. 27(a)]—shows an extensive diffusive field, with a small temperature gradient at the solid-liquid interface. Starting from a homogeneous temperature in the resting liquid with the crystal and the vessel surface at T_m and T_∞, a relaxation process is observed that settles to a buoyancy-driven streaming along the capillary within 8 min. The temperature field looks different under the influence of the convective flow [Fig. 27(b)]. The latent heat is transported away very effectively by the liquid xenon; the temperature gradient at the crystal surface is large. The upward xenon stream is strong around the capillary, but drives only a very weak flow in the rest of the vessel. The latent heat is removed from the growth vessel by the surrounding heat bath. Only a very small gradient exists in the vessel at some distance from the crystal. It is of the same order of magnitude as measured in our experiments.

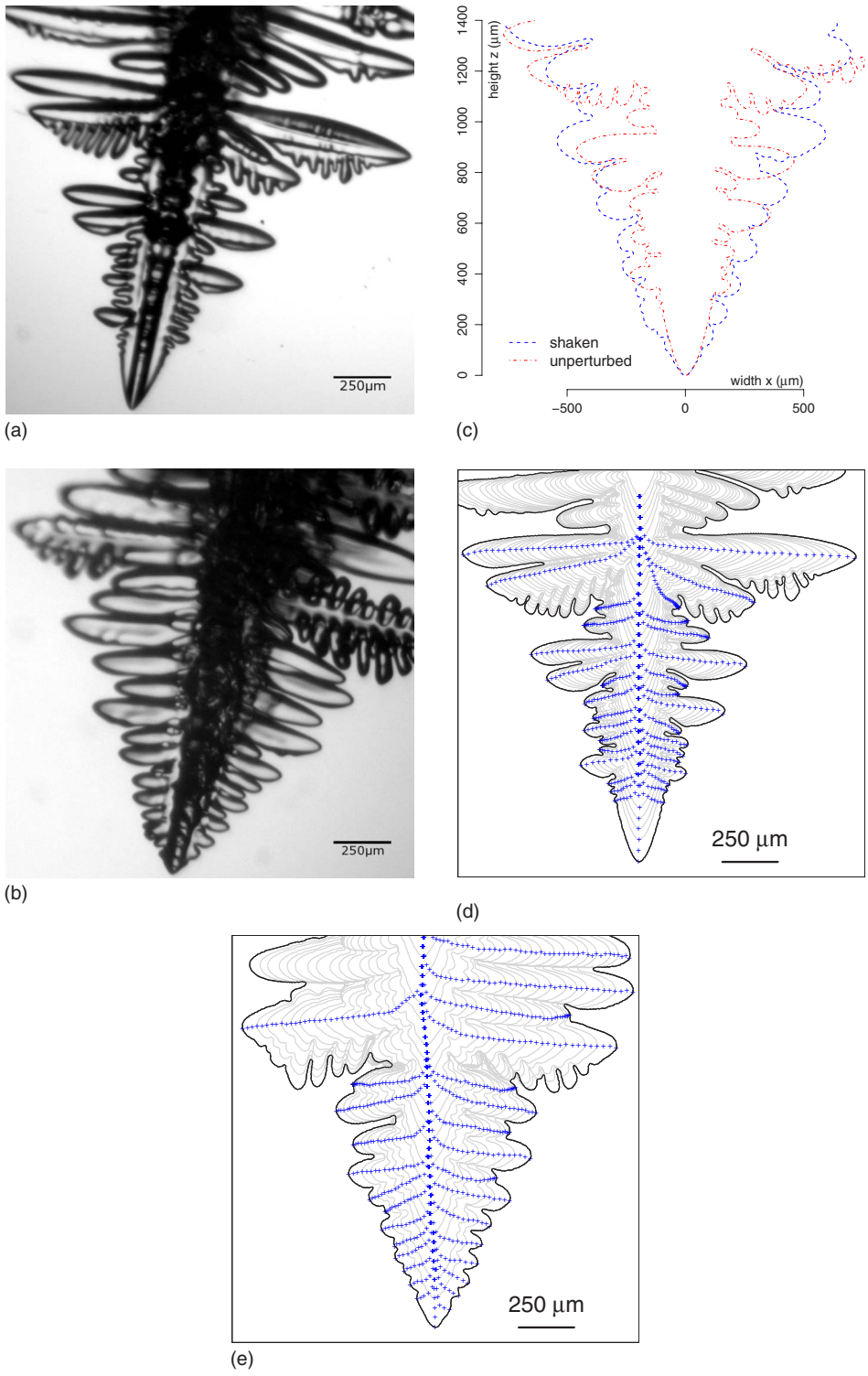

FIG. 24. (Color online) A comparison between a freely grown (a) and a shaken (b) dendrite. The shaken one is identified by eye to be thicker. The plot of the geometrically corrected contours (c) proves that this is not because of different projection angles. The sidebranches are tracked in (d), (e) and show a larger spacing and a less effective coarsening for the shaken dendrite (e).

The temperature and the flow velocity at a point 0.3 mmahead of the main tip are presented in Table III for three undercoolings in the range of the experiments. The maximum flow velocity at this point is of the order of magnitude of the observations.

C. Heating and cooling

Within this computational framework a complete heating cycle has been calculated. When a steady state had evolved after about 8 min, the heater was switched on for t_{on}=45 s and heating was interrupted for another t_{int}=15 s, typical in-

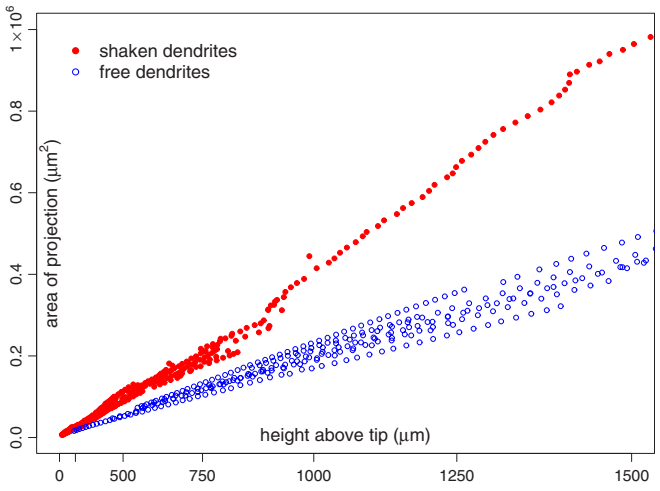

FIG. 25. (Color online) The area of the projection of a dendrite as function of the height. The values on the abscissa indicate the true height h of the dendrites. They are plotted squared to see the filling factor β from $A=\beta h^2$ as the slope. The area for the shaken crystals (●) grows faster with increasing height (i.e., the filling factor β is larger) than it does for free growth (○). There are 19 sequences of 12 different crystals shown; the undercoolings are between 100 mK and 250 mK for both the free and shaken ones. No significant influence of the undercooling is found.

tervals used in the experiments. The formation of complex flow patterns is observed. A snapshot of the situation after the tenth heating pulse is shown in Fig. 28. The flow around the crystal is found to change its velocity and its direction within seconds.

The resulting temporal evolution of the temperatures in the vessel is shown in Fig. 29. The four positions correspond to the real positions of the crystal tip, the 0.3-mm point, and the two Pt-100 resistors in the growth vessel, respectively. Compared with the experimental data, a good qualitative agreement is found.

TABLE I. The essential parameters used in the simulations.

Calculation parameters		
Time step	Δt	0.5 s
Cell diameter	Δx	≥ 20 μm
Domain dimensions	$l\times w\times h$	$5\times 5\times 5$ cm^3
Material parameters for liquid xenon		
Density[a]	ρ	2963 kg/m^3
Viscosity[a]	η_s	0.00057 kg/m s
Volume thermal expansion[b]	γ	0.0027 1/K
Heat capacity[c]	c_m	340 J/kg K
Thermal conductivity[d]	a	0.0734 W/m K

[a]Reference [63].
[b]Reference [64].
[c]References [63,65].
[d]Reference [66].

TABLE II. The mesh sizes for the finite-element simulations. The repeated heating cycles have been solved on the medium-resolution mesh because of hardware limitations.

Mesh	No. nodes	No. elements
3D medium res.	33334	176580
3D high res.	74780	405546

VI. DISCUSSION

A. Mechanism for tip splittings

The so-called tip splittings in the dendritic growth lead from a single dendrite to dendritic doublons, triplons, or quadruplons in a single step. Further splittings of the newly born tips result in higher-order multitip configurations. In the fcc structure of xenon, the occurrence of a split to three is a symmetry break. Compared to the self-organized triplets found numerically by Abel *et al.* [43] under the restriction of periodic BCs, we find these splittings in free growth. We propose a mechanism for the tip splittings based on the fact that free dendrites look like a rotational symmetric needle crystal in the foremost part. The fins become visible and the trunk evolves at a distance of about 3 tip radii from the tip; the sidebranches grow on the fins, starting about 10–15 tip radii behind the tip. This shape is clearly seen in Fig. 30.

As a reaction to a perturbation, the tip velocity decreases but the fins do not keep the distance to the tip; rather, they "catch up" with the main tip. In the usual maximum-area projection and outline investigation the tip becomes slower and thicker. The fins can even surpass the former "main" tip and evolve in two lobes. These structures then grow into new tips. An image sequence of the transition towards a doublon is shown in Fig. 31. A comparison with the tip-splitting mechanism in (quasi) two dimensions is shown in the contours in Fig. 32.

The same process can lead to quadruplons. In this case, all four fins surpass the main tip and four new tips are formed

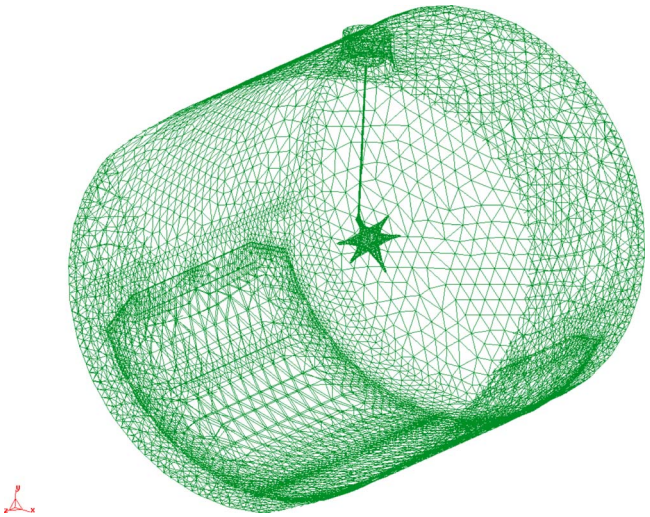

FIG. 26. (Color online) The boundary elements of the medium-resulotion mesh used in three dimensions. One part was cut away in this representation for a better view inside the vessel.

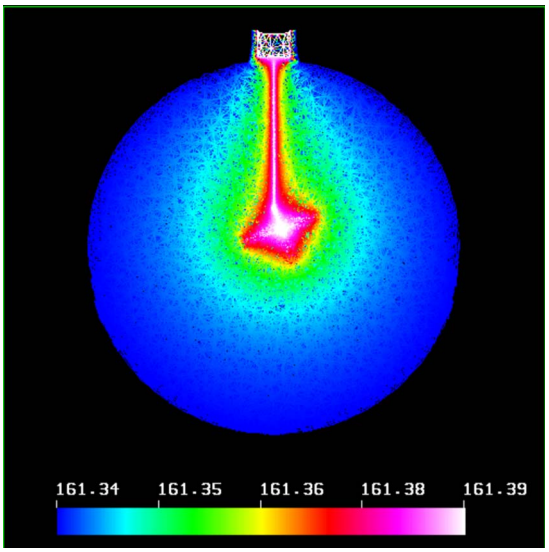

(a)

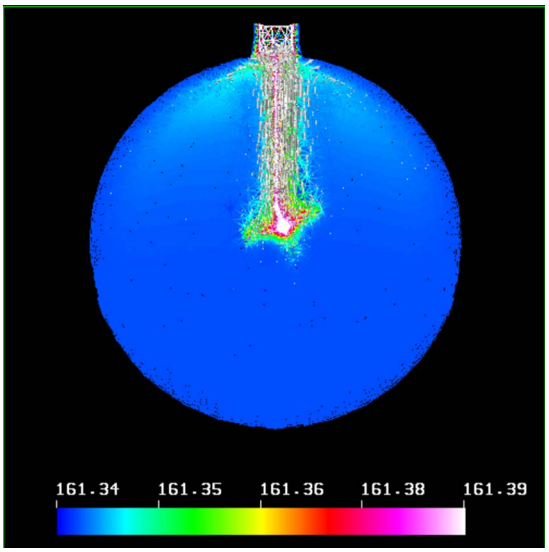

(b)

FIG. 27. (Color online) The solution for the temperature field in the growth vessel without any convection (a) and with convection (b). The undercooling at the outer boundary is ΔT=50 mK; the temperature on the crystal surface is T_m=161.3987 K. The crystal orientation is the same as in Fig. 26.

[see Fig. 33(a)]. The triplon is a degenerated quadruplon, where one of the four fins is surrounded by a slightly warmer melt due to convective flow. It grows a little slower and cannot evolve in a new tip. This is shown in Fig. 33(b). After some minutes of growth, the described process can repeat on one of the new tips, leading to the odd multitip configurations.

This mechanism is presumably different from how the tip splitting happens in directional solidification in quasi two dimensions, where in fact a "splitting" is observed (e.g., in Ref. [60]) and calculated (e.g., in Ref. [43]). Still it seems to be the same process of "splitting" into two, three, and four new tips observed in three-dimensional directional solidification experiments (e.g., in [67,68]).

TABLE III. The calculated values for the absolute velocity V_{abs} in μm/s and the temperature T in K at a point 0.3 mm ahead of the tip.

ΔT	~50 mK		~200 mK		~400 mK	
T_∞	161.3400 K		161.2000 K		161.0000 K	
	V_{abs}	T	V_{abs}	T	V_{abs}	T
Purely diffusive		161.3782		161.3457		161.2994
Natural convection	159	161.3652	306	161.2956	449	161.1970

B. Stabilized sidebranching

The shaking perturbations are thought to act on the diffusive field around the tip as shown in Fig. 34(a). The *compression* of the isotherms around the crystal along the oscillation direction causes a steeper temperature gradient to the luff side at the fins in or close to the plane of vibratory movements. The situation on the other lee side is more difficult. The perturbation amplitude is too small to cause a large-scale streaming around the crystal as it has been investigated by Tatsuno [69]. An important feature is a density change (number density of atoms) in the melt in the close vicinity of the former solid-liquid interface, caused by moving the crystal rapidly out of this region. The liquid xenon flows towards the former location of the crystal and compresses the isotherms that way, causing faster growth. The fins perpendicular to the plane of movement are shifted in

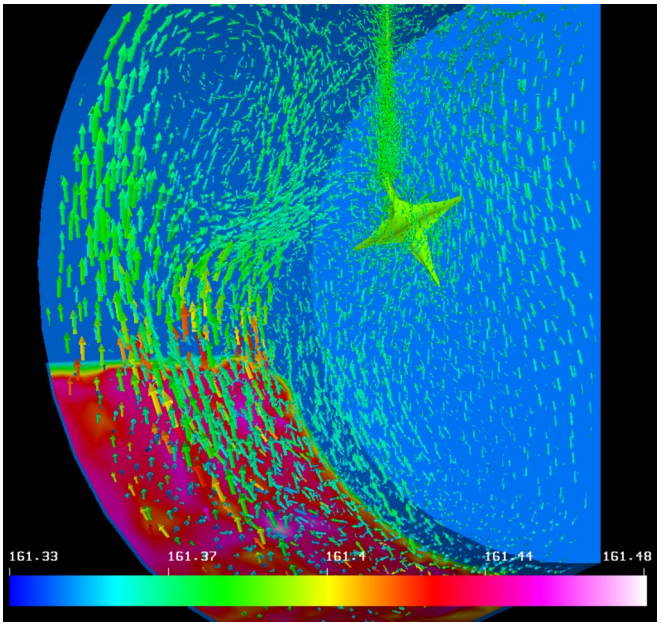

FIG. 28. (Color online) The flow and temperature in the growth vessel around the crystal after the tenth heating pulse. The length of the arrows shows the absolute velocity; the colors show the temperature. The crystal is found to be in a flow of xenon at about the melting temperature (same color as the crystal) from various directions.

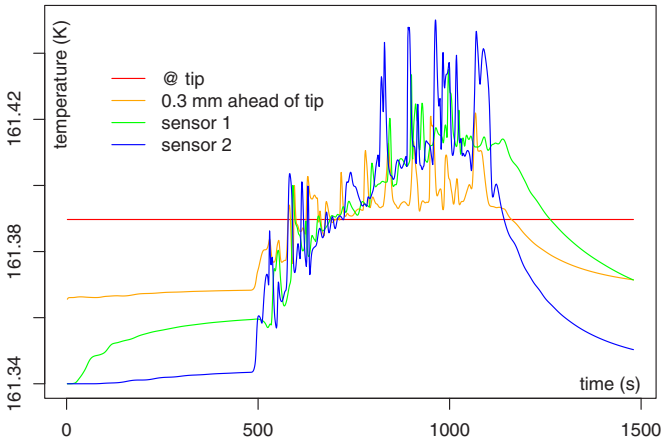

FIG. 29. (Color online) The temperatures as calculated at four points in the growth vessel. The points "sensor 1" and "sensor 2" correspond to the approximate position of the Pt-100 resistors in the experiment.

the diffusion field, and the isotherms are compressed, making the gradient steeper. A schematic representation is shown in Fig. 34(b). Thus shaking increases the growth rate on all sides. All sidebranches in the tip region grow with almost the same velocity. Starting from the very tip they build a front where none of them can escape from. Coarsening is suppressed as a direct consequence. The steeper gradient makes them grow faster than the unperturbed ones observed in free growth. This mechanism, however, should be examined in more detail in numerical simulations.

C. Synchronization of sidebranches: Heat transfer as coupling mechanism

Cascading tip splittings described in Sec. IV C are a strong indicator for a metastable oscillatory growth mode as proposed by Holzmann [12] and by Langer and Müller-Krumbhaar [47]. The thermal fluctuations that have been found to be too small for the observed sidebranch amplitudes [8,29] might be strong enough to drive the system behavior away from a fix point into the basin of attraction of a limit cycle. The emergence of symmetry in spatially separated regions of the crystal observed in restarted growth might be explained that way. The growth mode for *all* tips (the main tip as well as the dominant sidebranch tips) during the transition from melting to growth becomes unstable and changes more or less synchronously towards a more stable mode (the operating point of marginal stability, for example). The effect of this synchronous change is clearly seen in Fig. 35, where four sidebranches show identical structures even if they are about 1 mm apart.

The temporal evolution leading to this structure is shown in Fig. 36 in 20-s intervals. The main stem as well as the sidebranches shows the spherelike isotropic growth (a). The main tip shows the *T*-type sidebranching (b), (c). The insta-

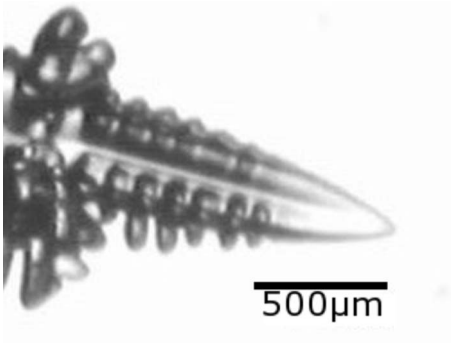

FIG. 30. The shape of a dendrite near the tip is clearly seen in this orientation. The tip is rotationally symmetric; the fins start about 3 tip radii behind and the sidebranches start growing on the fins about 15 tip radii behind the tip.

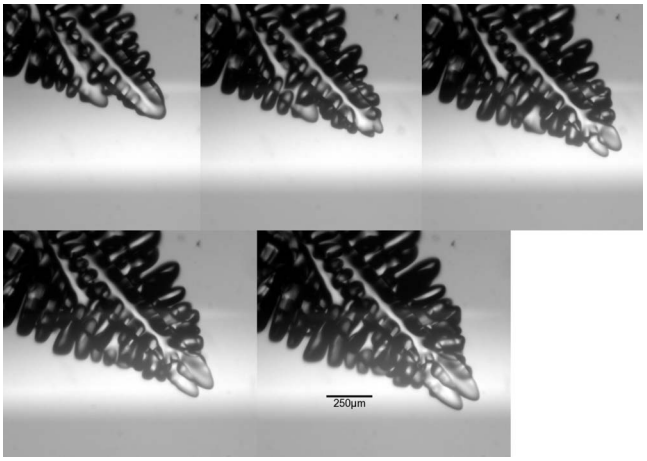

FIG. 31. The single-tip dendrite transforms into a doublon at the fins surpassing the main tip as is seen in the temporal evolution covering 482 s. The fins "catch up" with the main tip and surpass it, evolving into two new tips. These continue to grow parallel and define a doublon (courtesy of Stalder [57]).

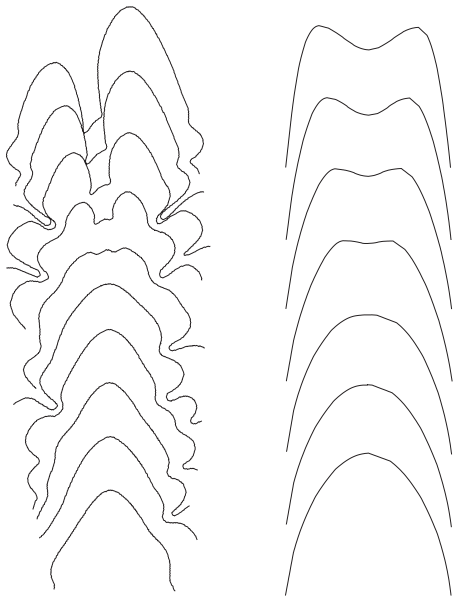

FIG. 32. Left: the projection of the tip splitting in three dimensions. The fins catch up with the main tip and surpass it, then evolve into new tips. Right: The tip splitting in two and quasi two dimensions. The tip grows large and becomes unstable.

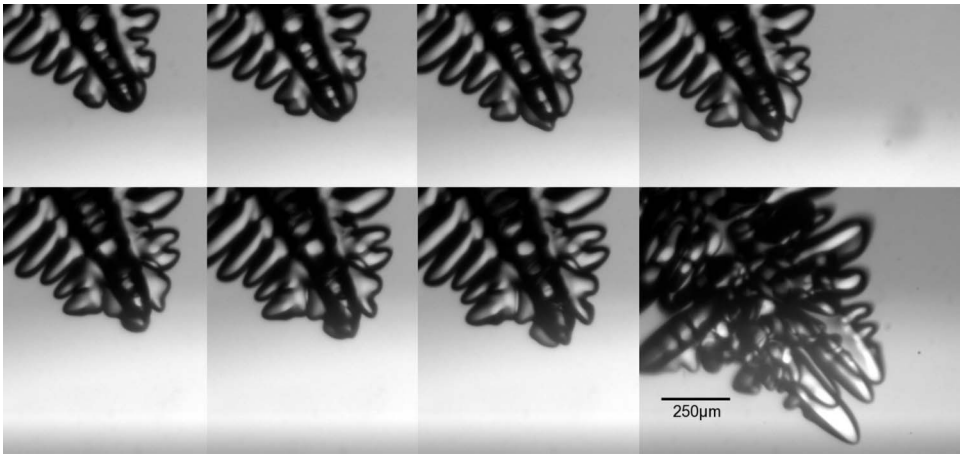

(a)

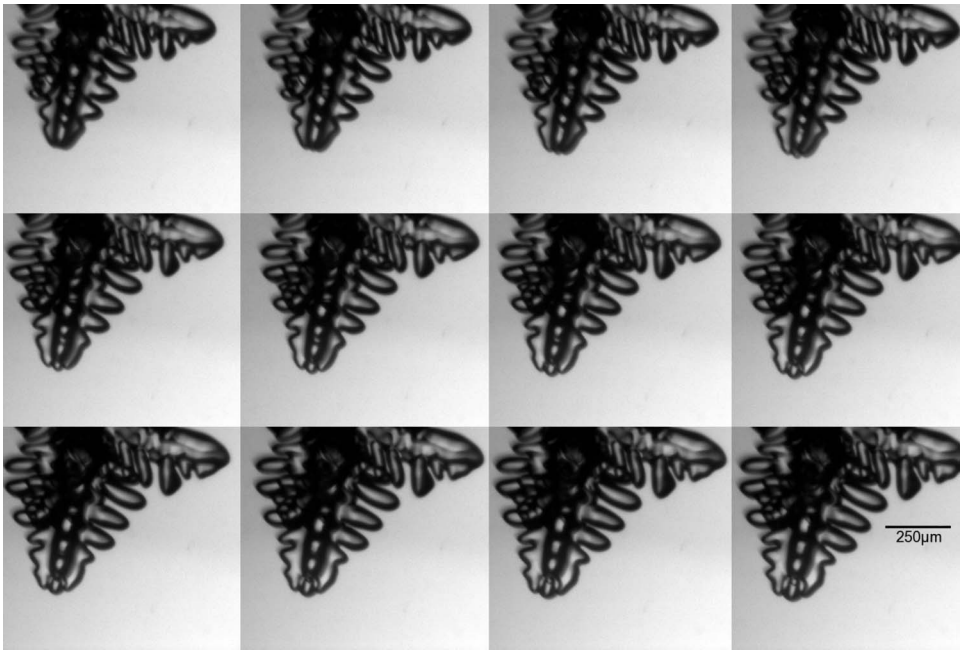

(b)

FIG. 33. (a) The transition from a single tip to a fourfold tip, called a quadruplon. The images are taken in an interval of 10 s. (b) A single tip transforms into a threefold tip, called a triplon. One of the fins in or out of the image plane does not evolve into a new tip. The images are in 6-s intervals.

bility at the main tip reaches the sidebranch tips about 20 s later and triggers a branching of all four of them (d). These higher-order branchings happen synchronously for up to minutes, leading to cascading structures described in Sec. IV C.

The idea of absolutely identical conditions and fluctuations around different tips so far apart seems not realistic. The crystal is inclined with respect to the gravitational field; thus, the convective flow on both sides is not identical either. Furthermore, the convective flow near the tip has been found (see Sec. V) to be of the order of magnitude of about 0.5 mm/s, which is about one order of magnitude too fast for the observed delay between main and sidebranches tips. Assuming the main tip is the most unstable region, then it will emit a small tip first (see Sec. IV A 1 b). This small tip has a higher curvature and thus a lower temperature as the original tip. The small tip will proceed into the melt with higher undercooling. Simultaneously heat will diffuse through the solid towards the small tip. Due to the high thermal diffusivity of the crystal ($D_{solid}:D_{liquid} \approx 7:1$), the whole crystal will become colder and thus drive the sidebranches away from their local equilibrium, making the sidebranch tips unstable and trigger the emission of new small tips.

The simultaneity of the system behavior of the four sidebranches is within the experimental observed delay time of $t=20$ s. With a thermal diffusivity in the solid of $D=D_{th}(s) \approx 4.96 \times 10^{-3}$ cm^2/s the expected distance for diffusion is estimated:

$$\langle x^2 \rangle = Dt \approx 1 \times 10^{-1} \text{ cm}^2, \tag{7}$$

$$\sqrt{\langle x^2 \rangle} \approx 3 \times 10^{-1} \text{ cm} = 3 \text{ mm}. \tag{8}$$

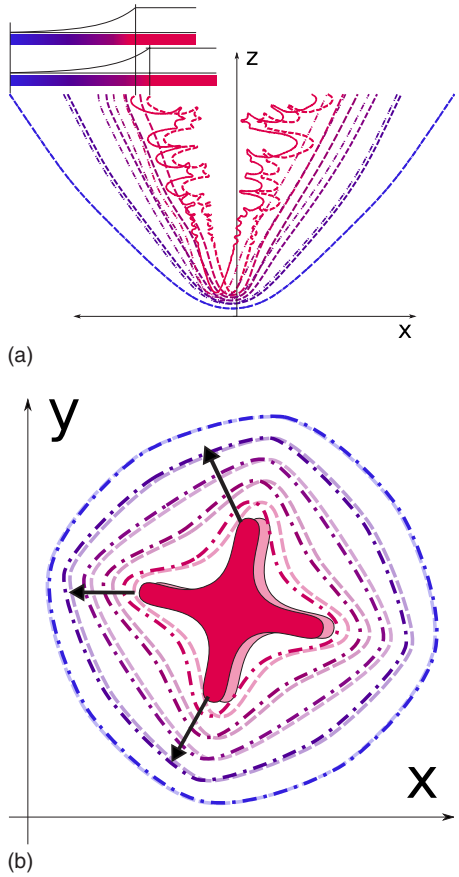

FIG. 34. (Color online) Shaking compresses the isotherms spacing in the shaking direction (parallel to the $-x$ axis in this representation). This results in a steeper gradient in the compression direction. The stretch of the isotherms in the other direction shows only the qualitative purely diffusive temperature field. It is thought that the density drop by moving the crystal causes a flow towards the new position and therefore compresses this isotherms too.

The diffusion speed in the solid phase seems to be compatible with the observations.

It might be that this mechanism is also active during the growth of other dendritic shapes—e.g., snow crystals. This would explain the high degree of symmetry of snow crystals.

D. Conclusion

The experimental findings presented in this paper show that the system behavior of the growing dendrite allows several operating states. Indications for a metastable limit cycle have been found, causing the periodic tip splittings and the fourfold-symmetric sidebranching as well as tip velocity oscillations.

Thermal noise as small perturbation seems to be the reason for one type of sidebranches (N-type) and for random and transient tip splittings. This noise can also drive the system into the limit cycle operating mode. In this framework, the experimentally [70,71] and numerically [72] observed, randomly showing-up sequences of 3–12 sidebranches starting synchronously and with unique spacing, so-called *bursts*, could be explained as transient limit cycle behavior of the system in free growth.

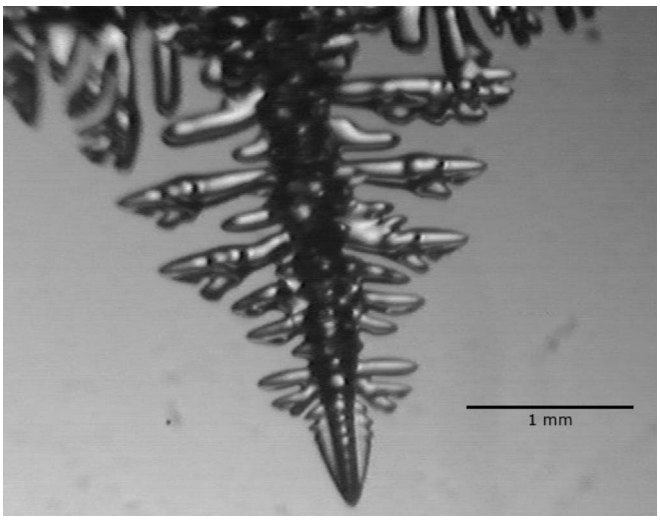

FIG. 35. The two dominant sidebranch pairs show the same structures at the same relative position in their growth. This means these structures have been generated synchronously even if the distance between the two sides is about 1 mm.

Still thermal noise seems not to be strong enough to drive the system into a stable multitip configuration. This mode can be stabilized by continuous external perturbations. Changes in the external forcing influence the kinetics near the solid-liquid interface causing inclinations and twists.

Large perturbations (heating pulses, melting, and large temperature drops) can drive the system out of any steady state. The relaxation back to a steady state reveals determin-

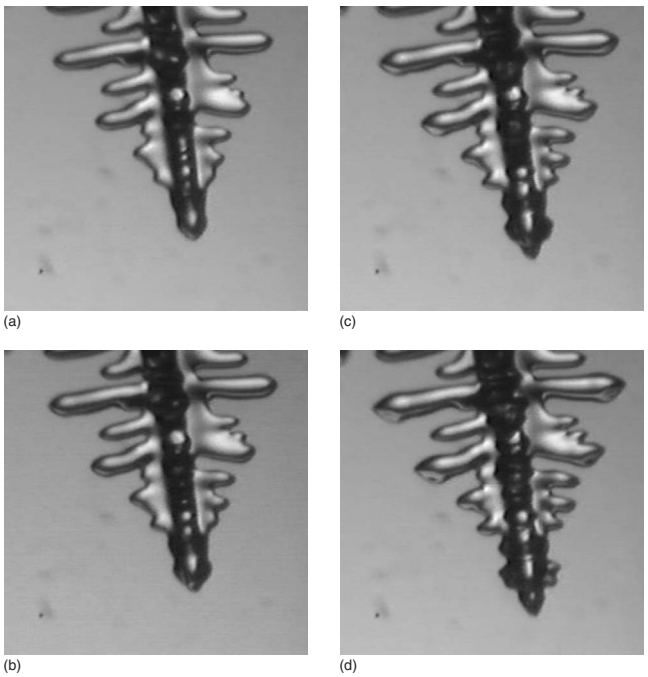

FIG. 36. The temporal evolution leading to the structures in Fig. 35. The spherelike transition of the main tip is mirrored in the behavior of the sidebranch tips with a lag of about 20 s. The sidebranches growing on both sides behave synchronously (within the detection limit).

istic behavior, such as the reproducible *T*-type sidebranches and the symmetry.

The mechanism of the fins surpassing the tip can explain the transition from a single tip with fourfold symmetry to either dendritic doublons, triplons, or quadruplons. By a sequential appearance of this mechanism, the odd five or more multitip configurations are explained.

The results of more than 30 melting experiments and 20 shaking experiments can serve as a benchmark for future computational and theoretical results in order to describe the transient crystal growth in large vessels. The complicated system behavior, determined by a point attractor (operating point), by a limit cycle, and by metastable multitip configurations, allows to control the characteristic growth parameters and therefore the shape of crystals. These findings might lead towards a dendrite engineering during solidification.

ACKNOWLEDGMENTS

We thank the members of the Laboratory for Solid State Physics, Professor K. Ensslin, Professor B. Batlogg, and Professor H.-R. Ott for their support of our experiments and G. Kreuzer and L. Mächler for their contributions. We appreciate the many discussions with H. Singer and his valuable numerical routines.

[1] F. C. Frank, Contemp. Phys. **23**, 3 (1982).
[2] M. E. Glicksman, M. B. Koss, and E. A. Winsa, Phys. Rev. Lett. **73**, 573 (1994).
[3] J. C. LaCombe, M. B. Koss, J. E. Frei, C. Giummarra, A. O. Lupulescu, and M. E. Glicksman, Phys. Rev. E **65**, 031604 (2002).
[4] H. Honjo, S. Ohta, and Y. Sawada, Phys. Rev. Lett. **55**, 841 (1985).
[5] U. Bisang and J. H. Bilgram, Phys. Rev. E **54**, 5309 (1996).
[6] J. H. Bilgram, M. Firmann, and E. Hürlimann, J. Cryst. Growth **96**, 175 (1989).
[7] E. Hürlimann, R. Trittibach, U. Bisang, and J. H. Bilgram, Phys. Rev. A **46**, 6579 (1992).
[8] A. Dougherty, P. D. Kaplan, and J. P. Gollub, Phys. Rev. Lett. **58**, 1652 (1987).
[9] A. Dougherty and R. Chen, Phys. Rev. A **46**, R4508 (1992).
[10] D. P. Corrigan, M. B. Koss, J. C. LaCombe, K. D. de Jager, L. A. Tennenhouse, and M. E. Glicksman, Phys. Rev. E **60**, 7217 (1999).
[11] J. S. Langer, in *Chance And Matter*, Les Houches, Session XLVI, 1986, edited by J. Souletie, J. Vannimenus, and R. Stora (Elsevier, Amsterdam, 1987), pp. 629–711.
[12] E. G. Holzmann, Ph.D. thesis, Stanford University, 1969.
[13] X. Tong, C. Beckermann, A. Karma, and Q. Li, Phys. Rev. E **63**, 061601 (2001).
[14] Y.-W. Lee, R. Ananth, and W. N. Gill, J. Cryst. Growth **132**, 226 (1993).
[15] K.-K. Koo, R. Ananth, and W. N. Gill, Phys. Rev. A **44**, 3782 (1991).
[16] S. Akamatsu, G. Faivre, and T. Ihle, Phys. Rev. E **51**, 4751 (1995).
[17] I. Stalder and J. H. Bilgram, Europhys. Lett. **56**, 829 (2001).
[18] B. T. Murray, A. A. Wheeler, and M. E. Glicksman, J. Cryst. Growth **154**, 386 (1995).
[19] H.-J. Diepers, D. Ma, and I. Steinbach, J. Cryst. Growth **237**, 149 (2002).
[20] A. Dougherty and T. Nunnally, J. Cryst. Growth **300**, 467 (2007).
[21] A. V. Gorbunov, Solid State Phenom. **23**, 15 (1992).
[22] A. Karma, Y. H. Lee, and M. Plapp, Phys. Rev. E **61**, 3996 (2000).
[23] G. P. Ivantsov, Dokl. Akad. Nauk SSSR **58**, 567 (1947).
[24] G. E. Nash and M. E. Glicksman, Acta Metall. **22**, 1283 (1974).
[25] J. S. Langer and H. Müller-Krumbhaar, Acta Metall. **26**, 1681 (1978).
[26] R. Pieters and J. S. Langer, Phys. Rev. Lett. **56**, 1948 (1986).
[27] M. N. Barber, A. Barbieri, and J. S. Langer, Phys. Rev. A **36**, 3340 (1987).
[28] D. A. Kessler, J. Koplik, and H. Levine, Adv. Phys. **37**, 255 (1988).
[29] J. S. Langer, Phys. Rev. A **36**, 3350 (1987).
[30] M. Ben Amar and E. A. Brener, Phys. Rev. Lett. **71**, 589 (1993).
[31] E. A. Brener, Phys. Rev. Lett. **71**, 3653 (1993).
[32] U. Bisang and J. H. Bilgram, Phys. Rev. Lett. **75**, 3898 (1995).
[33] E. A. Brener and D. Temkin, Phys. Rev. E **51**, 351 (1995).
[34] O. Wittwer and J. H. Bilgram, Phys. Rev. E **74**, 041604 (2006).
[35] E. A. Brener, K. Kassner, H. Müller-Krumbhaar, and D. Temkin, Int. J. Mod. Phys. C **3**, 825 (1992).
[36] E. A. Brener, H. Müller-Krumbhaar, and D. Temkin, Europhys. Lett. **17**, 535 (1992).
[37] E. A. Brener, H. Müller-Krumbhaar, and D. Temkin, Phys. Rev. E **54**, 2714 (1996).
[38] H. M. Singer, I. Singer-Loginova, J. H. Bilgram, and G. Amberg, J. Cryst. Growth **296**, 58 (2006).
[39] E. A. Brener, T. Ihle, H. Müller-Krumbhaar, Y. Saito, and K. Shiraishi, Physica A **204**, 96 (1994).
[40] T. Ihle and H. Müller-Krumbhaar, Phys. Rev. Lett. **70**, 3083 (1993).
[41] T. Ihle and H. Müller-Krumbhaar, Phys. Rev. E **49**, 2972 (1994).
[42] U. Lappe, Ph.D. thesis, KFA Jülich, Jülich, Germany (1980).
[43] T. Abel, E. A. Brener, and H. Müller-Krumbhaar, Phys. Rev. E **55**, 7789 (1997).
[44] E. Raz, S. G. Lipson, and E. Polturak, Phys. Rev. A **40**, 1088 (1989).
[45] S. Liu, S.-Z. Lu, and A. Hellawell, J. Cryst. Growth **234**, 751 (2002).
[46] M. E. Glicksman, J. S. Lowengrub, and S. Li, in *Modeling Of Casting, Welding And Advanced Solidification Processes XI*, edited by C.-A. Gandin and M. Bellet (The Minerals, Metals & Materials Society, Warrendale, PA, 2006), pp. 521–528.

[47] J. S. Langer and H. Müller-Krumbhaar, Phys. Rev. A **27**, 499 (1983).
[48] R. K. Trivedi and J. T. Mason, Metall. Trans. A **22**, 235 (1991).
[49] M. E. Glicksman, R. J. Schaefer, and J. D. Ayers, Metall. Trans. A **7**, 1747 (1976).
[50] H. M. Singer and J. H. Bilgram, J. Cryst. Growth **261**, 122 (2004).
[51] A. Dougherty and M. Lahiri, J. Cryst. Growth **274**, 233 (2004).
[52] H. M. Singer and J. H. Bilgram, Phys. Rev. E **69**, 032601 (2004).
[53] M. B. Koss, J. C. LaCombe, A. Chait, V. Pines, M. Zlatkowski, M. E. Glicksman, and P. Kar, J. Cryst. Growth **279**, 170 (2005).
[54] I. Steinbach, H.-J. Diepers, and C. Beckermann, J. Cryst. Growth **275**, 624 (2005).
[55] M. E. Glicksman, A. O. Lupulescu, and M. B. Koss, J. Thermophys. Heat Transfer **17**, 69 (2003).
[56] A. O. Lupulescu, M. E. Glicksman, and M. B. Koss, J. Cryst. Growth **276**, 549 (2005).
[57] I. Stalder, Ph.D. thesis, Laboratorium für Festkörperphysik, ETH Zürich, Zürich, 2000.
[58] O. Wittwer, Ph.D. thesis, Laboratorium für Festkörperphysik, ETH Zürich, 2006.
[59] S. Henry, T. Minghetti, and M. Rappaz, Acta Mater. **46**, 6431 (1998).
[60] B. Utter, R. Ragnarsson, and E. Bodenschatz, Phys. Rev. Lett. **86**, 4604 (2001).
[61] A. Karma and A. E. Lobkovsky, Phys. Rev. Lett. **92**, 245510 (2004).
[62] M. Dorn-Aymon, Master's thesis, Laboratorium für Festkörperphysik, ETH Zürich, 2003.
[63] P. Malbrunot, A. Boyer, E. Charles, and H. Abachi, Phys. Rev. A **27**, 1523 (1983).
[64] A. J. Leadbetter and H. E. Thomas, Trans. Faraday Soc. **61**, 10 (1965).
[65] *Selected Values Of The Thermodynamic Properties Of The Elements* (American Society For Metals, Metals Park, OH, 1973).
[66] *Thermophysical Properties Of Matter*, Vol. 3 of TPRC Data Series (IFI/Plenum, New York, 1970).
[67] C. Weiss, N. Bergeon, N. Mangelinck-Noël, and B. Billia, Mater. Sci. Eng., A **413**, 296 (2005).
[68] B. Billia (private communication).
[69] M. Tatsuno, J. Phys. Soc. Jpn. **50**, 330 (1981).
[70] M. Georgelin and A. Pocheau, Phys. Rev. E **57**, 3189 (1998).
[71] M. Georgelin, S. Bodea, and A. Pocheau, Europhys. Lett. **77**, 46001 (2007).
[72] M. Plapp (private communication).